Master's thesis
Space Physics

Foreshock Compressive Structures as the Cause of Magnetosheath Jets

Jonas E. Suni

March 30, 2021

Supervisor(s): prof. Minna Palmroth

Censor(s): prof. Minna Palmroth
prof. Tomas Karlsson (KTH Stockholm)

UNIVERSITY OF HELSINKI
Master's Programme in Particle Physics and Astrophysical Sciences
P.O. Box 64 (Gustaf Hällströmin katu 2) FI-00014 University of Helsinki

HELSINGIN YLIOPISTO — HELSINGFORS UNIVERSITET — UNIVERSITY OF HELSINKI

Tiedekunta — Fakultet — Faculty	Koulutusohjelma — Utbildningsprogram — Education programme
Faculty of Science	Master's Programme in Particle Physics and Astrophysical Sciences

Tekijä — Författare — Author
Jonas E. Suni

Työn nimi — Arbetets titel — Title
Foreshock Compressive Structures as the Cause of Magnetosheath Jets

Opintosuunta — Studieinriktning — Study track
Space Physics

Työn laji — Arbetets art — Level	Aika — Datum — Month and year	Sivumäärä — Sidoantal — Number of pages
Master's thesis	March 30, 2021	53 pages

Tiivistelmä — Referat — Abstract

Magnetosheath jets are a class of structures in the Earth's magnetosheath usually defined by an enhancement of the dynamic pressure of the plasma. Magnetosheath jets have been observed by several different spacecraft over the past few decades, but their origin and formation mechanism have remained unclear. The aim of this thesis is to use data from a global simulation to investigate the origin of magnetosheath jets.

We defined two different kinds of structures, magnetosheath jets and foreshock compressive structures (FCS), and collected a database of individual jets and FCSs from 4 Vlasiator global hybrid-Vlasov simulation runs, all of which simulate only the ecliptic plane. We then conducted a statistical analysis of the properties of jets and FCSs, and their occurrence rates as a function of the definition of the FCS criterion. Jets were separated into two categories: jets that form in contact with FCSs (FCS-jets), and those that do not (non-FCS-jets).

We found that up to 75% of magnetosheath jets form in association with an FCS impacting the Earth's bow shock. We also found that FCS-jets penetrate deeper into the magnetosheath than non-FCS-jets. Finally, we found no conclusive explanation for the formation of non-FCS-jets.

The properties of both jets and FCSs agree qualitatively and to some extent quantitatively with spacecraft observations and other simulations in the literature. The formation of jets from FCSs impacting the bow shock is similar to the proposed theory that jets are linked to Short Large-Amplitude Magnetic Structures (SLAMS).

In the future, we will study magnetosheath jets and FCSs in polar plane simulation runs as well, and ultimately in full 3D simulation runs. If made possible by new simulations, the effects of electron kinetic effects on jets and FCSs will also be studied. Comparison studies with spacecraft observations of jet formation from FCSs will also be conducted, if and when such observations are found and become available.

Avainsanat — Nyckelord — Keywords
Space physics, Foreshock, Bow shock, Magnetosheath, Magnetosheath jets, Vlasiator

Säilytyspaikka — Förvaringsställe — Where deposited

Muita tietoja — övriga uppgifter — Additional information

Contents

1. Introduction

1.1 The Sun and the Earth's Magnetic Field

This study focuses on interaction between the Earth's foreshock and magnetosheath, but to put these two regions into context, a general introduction to near-Earth space is required. Figure 1.1 shows an overview of different regions in near-Earth space. Aside from the tail plasma sheet (which is not of importance for this study), these regions will be introduced in this section. We first explain the origin of the solar wind and interplanetary magnetic field. Next, we give a general introduction to shocks, after which we explain the foreshock concept. We introduce the bow shock and magnetosheath as well as sheath flow mechanics. Finally, we introduce the magnetopause and magnetosphere.

1.1.1 The Solar Wind

The Sun emits electromagnetic radiation, which is readily visible as sunlight on Earth during the day. But the solar corona is also the source of a high-speed stream of hot charged particles that we call the solar wind. The temperature of the solar corona is $\sim 10^6$ K, which is too high for a hydrostatic equilibrium to form between the corona and interstellar space. Instead, the corona is in hydrodynamic equilibrium, constantly expanding outward. Close to the sun, the velocity of the solar wind increases with distance from the sun, and it becomes supersonic before it reaches

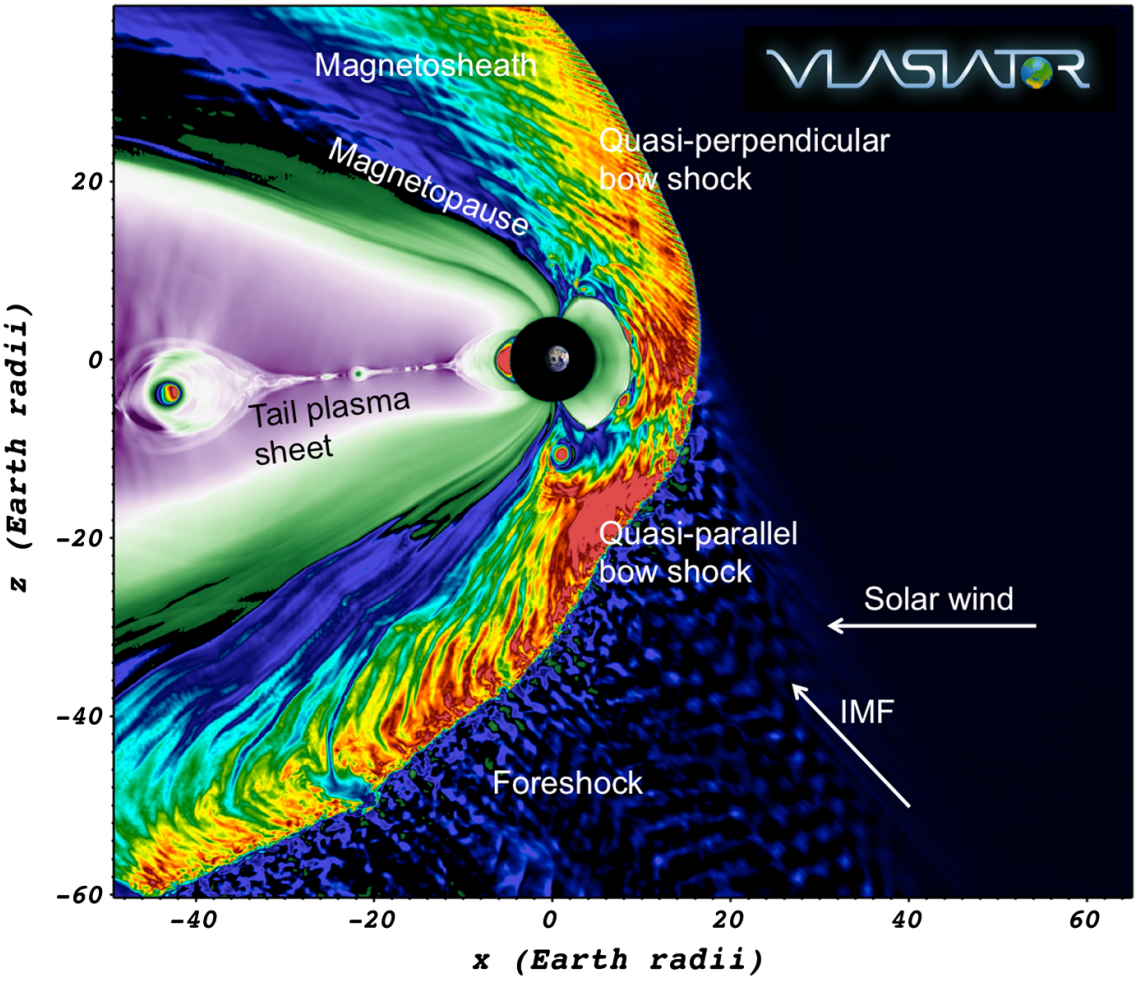

Figure 1.1: Global view of a Vlasiator simulation run in the GSE XZ-plane, showing different regions of near-Earth space. The coordinate system used is the Geocentric Solar Ecliptic (GSE) system, where +X points sunward, +Z points toward ecliptic north, and Y completes the right-handed system. The arrows indicate the solar wind and IMF directions. From Palmroth et al. (2018a).

the orbit of the Earth (Parker, 1958). The frequency of collisions between particles in the solar wind is low - we call the solar wind a collisionless plasma. The fact that the Earth has a magnetic field is common knowledge to anyone who has used a compass, but the Sun also has a magnetic field, which fills the corona. Magnetised collisionless plasmas exhibit a phenomenon where the plasma and magnetic field move together. This is known as the frozen-in condition or Alfvén's theorem

(Koskinen, 2011). As the solar wind flows outward from the Sun through the Solar System, it pulls the solar magnetic field with it, filling the Solar System with the so called Interplanetary Magnetic Field (IMF). This IMF, and the solar wind, then interact with the Earth's magnetic field (e.g. Dungey 1961).

1.1.2 The Foreshock

When a flow encounters a flow obstacle, the flow is diverted around the obstacle. The change in flow direction around the obstacle is gradual, and it is facilitated by the fact that information about the obstacle travels upstream in the form of disturbances that propagate at the characteristic signal speed of the medium. If the flow is supersonic, i.e. the flow velocity exceeds the signal speed of the medium, the disturbances cannot propagate upstream at the signal speed, and the flow cannot receive information about the obstacle necessary for diverting the flow. This problem is remedied by the formation of a shock front upstream of the obstacle, at which the flow is slowed to subsonic speeds, energy is dissipated, and other flow properties change abruptly. The changes in flow density, velocity, and pressure (and temperature) are described by a set of equations called the Rankine-Hugoniot jump conditions. These conditions, derived from the continuity equation of hydrodynamics, ensure the conservation of mass, momentum and energy across the shock.

Shocks of this kind are readily observed on Earth when an airplane exceeds the speed of sound of air, but the general description also applies to collisionless, magnetised plasmas. In this case, the flow dynamics can be described using magnetohydrodynamics (MHD). In the MHD description, plasma is modeled as a fluid as in the hydrodynamic description, but with additional magnetic terms in the momentum and energy transport equations, as well as in the definition of the total energy itself. In addition, the magnetic field itself is transported along with the flow. From the MHD equations, one can derive the MHD Rankine-Hugoniot jump conditions,

which ensure the conservation of magnetic flux density as the flow crosses the shock. The MHD Rankine-Hugoniot conditions have several different solutions (Kivelson and Russell, 1995).

The solutions to the Rankine-Hugoniot jump conditions can be divided into two main categories: Discontinuities and (true) shocks. Contact and tangential discontinuities are characterised by the lack of any flow across the discontinuity, and in the tangential case the magnetic field is also perpendicular to the discontinuity on both sides. In a rotational discontinuity, there is a change of direction but not magnitude of both velocity and magnetic flux across the discontinuity. Shocks, on the other hand, are characterised by compression and dissipation as well as a decrease of the flow speed component parallel to the shock normal as the flow crosses the discontinuity. Shocks can also be separated according to the angle, θ_{Bn}, between the upstream magnetic field direction and the shock normal. In a parallel shock, $\theta_{Bn} = 0°$, and the magnetic field is unchanged as the flow crosses the shock. In a perpendicular shock, $\theta_{Bn} = 90°$, and the plasma pressure and magnetic field strength increase across the shock. Shocks that are neither parallel nor perpendicular are called oblique shocks, and they can be further divided into different types. In a fast-mode shock, the plasma pressure and magnetic field strength increase across the shock, and the angle between the downstream magnetic field and the shock normal is larger than θ_{Bn}. In a slow-mode shock, the plasma pressure increases but the magnetic field strength decreases, and the angle between the downstream magnetic field and the shock normal is smaller than θ_{Bn}. Intermediate shocks are very similar to rotational discontinuities, and when the plasma is isotropic, the two are identical.

The Earth's magnetic field functions as a flow obstacle to the incoming solar wind, and a bow shock forms where the solar wind flow speed falls below the Alfvén velocity $v_A = B/\sqrt{\mu_0 mn}$, where B is the magnetic field strength, μ_0 is the vacuum permeability, n is particle density, and m is particle mass. Earth's bow shock is a

fast-mode shock, so the density and pressure of the plasma increase across the shock, the flow velocity decreases, and the magnetic field becomes more tangential to the shock on the downstream side. The shock is also supercritical, which means that the heating and compression of the plasma as it crosses the shock cannot dissipate enough of the upstream energy. Energy must thus be dissipated in other ways as well, such as reflection of particles by the shock. Charged particles in magnetic fields gyrate around the field lines, and when they encounter a gradient in the magnetic field, they experience a force anti-parallel to the gradient. This force can result in the reflection of particles, an effect called a magnetic mirror (Koskinen, 2011). This way, solar wind particles can be reflected at the bow shock. These reflected particles then move upstream back into the solar wind along the magnetic field lines (Thomsen et al., 1983). The backstreaming particles interact with the solar wind, causing plasma instabilities, which excite waves (Hoppe et al., 1981). One example is the right hand ion-ion beam instability, which excites ultra-low frequency (ULF) "30-second" waves with periods on the order of tens of seconds (Eastwood et al., 2005). These waves propagate sunward in the plasma frame of reference, but because the solar wind is supersonic, the waves are advected with the solar wind flow back to the bow shock. As they approach the bow shock, the waves steepen. The upstream region containing reflected particles and waves is called the foreshock (see Figure 1.1), and because the reflected particles move along magnetic field lines, the foreshock is located upstream from the part of the bow shock where the shock normal and magnetic field are not perpendicular to each other. The foreshock waves interact with the bow shock and affect the region downstream of the bow shock, which is called the magnetosheath.

1.1.3 The Bow Shock and the Magnetosheath

As the solar wind flow crosses the bow shock, the plasma is abruptly compressed and heated according to the Rankine-Hugoniot conditions as the flow velocity component parallel to the shock normal decreases from supersonic to subsonic. Because the bow shock is roughly paraboloid in shape, the upstream magnetic field-shock normal angle θ_{Bn} is different at different parts of the shock. The part where $\theta_{Bn} < 45°$ is called the quasi-parallel bow shock, and the part where $\theta_{Bn} > 45°$ is called the quasi-perpendicular bow shock. These two parts of the bow shock behave quite differently. So called kinetic effects, such as the reflected backstreaming particles in the foreshock, are significant upstream of the quasi-parallel shock. The waves in the foreshock are advected to the quasi-parallel shock and can cause it to ripple, causing θ_{Bn} to change locally (Schwartz and Burgess, 1991). Downstream of the bow shock, the shocked solar wind plasma flowing around the obstacle posed by the Earth's magnetic field forms the region of space known as the magnetosheath (Figure 1.1).

The flow of shocked solar wind plasma around a magnetised planet, such as Earth, depends on the magnetic pressure $p_{mag} = B^2/2\mu_0$ of the Earth's magnetic field B and the total pressure $P_{tot} = P_{th} + P_{mag} + P_{dyn}$ of the solar wind plasma, where $P_{th} = \gamma n k_B T$ is the thermal pressure, $P_{dyn} = mnv^2$ is the dynamic pressure, γ is the polytropic index, k_B is Boltzmann's constant, T is temperature, and v is flow velocity. Spreiter and Stahara (1980) developed a computational model for the plasma flow and magnetic field in the magnetosheath as a function of the solar wind properties. This is a magnetogasdynamic model, where the solar wind plasma beta $\beta = P_{th}/P_{mag}$ is assumed to be large and thus the solar wind magnetic pressure is neglected in the calculation of the pressure balance between the solar wind and the Earth's magnetic field. The flow of the sheath plasma around the obstacle is calculated first, and then the magnetic field is advected along this flow to give the sheath magnetic field. In reality, the solar wind magnetic pressure does play a part

in the sheath flow dynamics. Figure 1.2 shows examples of the streamlines, i.e. the paths along which plasma parcels move, resulting from this model.

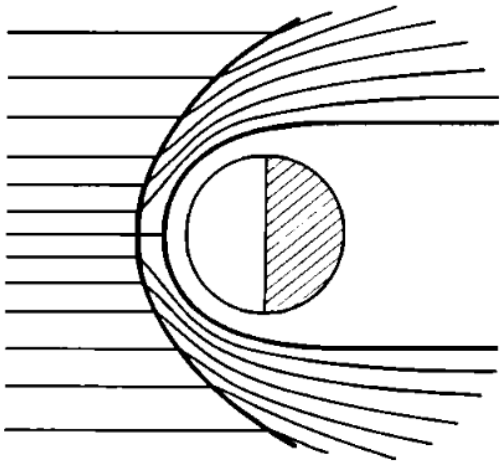

Figure 1.2: Magnetosheath streamlines calculated using the Spreiter and Stahara (1980) model. From Luhmann (1991).

Like the bow shock, the magnetosheath can be roughly divided into two parts: The quasi-parallel magnetosheath and the quasi-perpendicular magnetosheath. Due to the interaction with the foreshock upstream of the quasi-parallel bow shock and the waves advecting into that part of the shock, kinetic effects are also important in the quasi-parallel magnetosheath. The inner earthward boundary of the magnetosheath is called the magnetopause (see Figure 1.1).

1.1.4 The Magnetopause and the Magnetosphere

The pressure of the solar wind compresses the dayside part of the Earth's magnetic field. At the subsolar point where the solar wind pressure and Earth's magnetic pressure are in balance, the earthward flow of the shocked solar wind plasma in the magnetosheath stagnates. The stagnation of the flow in a magnetic field causes the formation of a current system known as the Chapman-Ferraro current (Koskinen, 2011) perpendicular to both the earthward magnetosheath flow and the Earth's

magnetic field. This current system forms the magnetopause boundary that serves to isolate the magnetosheath plasma from the region earthward of the inner boundary of the sheath, which is known as the Earth's magnetosphere. The near-subsolar parts of the magnetopause form a tangential discontinuity. On the nightside of the Earth, the Chapman-Ferraro currents connect to each other to form a closed current system, and the magnetic field induced by these return currents elongates the nightside part of the Earth's magnetic field into a magnetotail (see Figure 1.1).

1.2 Foreshock structures

As mentioned before, particles reflected back upstream from the bow shock interact with the solar wind and cause plasma instabilities, which excite many kinds of waves. Of particular interest are the "30-second" waves, as they are the most commonly observed wave type in the foreshock, and they are associated with wave steepening and the formation of structures.

In this study, we are interested in structures that exhibit stronger magnetic field compared to the IMF. This structure type can be roughly divided into two categories: Shocklets (Hoppe et al., 1981) and Short Large-amplitude Magnetic Structures, or SLAMS for short (Schwartz and Burgess, 1991). Shocklets appear to be like small shocks or steepening ULF waves and are defined as having modest magnetic field enhancements, < 2 times the ambient solar wind value. Schwartz (1991) estimated steepened ULF waves to have wavelengths and thus scale sizes on the order of 1 R_e (Earth radii), which corresponds to approximately 6371 km. This is supported by Lucek et al. (2002), who found the steepened ULF wave scale sizes to be much greater than 1000 km.

SLAMS appear as coherent isolated structures with magnetic field enhancements between 3 and 5 times the ambient solar wind value. Schwartz (1991) estimates SLAMS to have dimensions of 0.5×1.0 R_e. However, Lucek et al. (2002,

2004, 2008) found that while SLAMS are coherent on length scales exceeding 1000 km, they exhibit significant variations of the magnetic field on smaller scales, and thus probably have smaller spatial extents than the steepened ULF waves/shocklets. Schwartz and Burgess (1991) suggested that as a SLAMS is advected toward the bow shock, its magnetic field grows and the upstream plasma between the structure and the bow shock is heated and compressed until it becomes similar to the downstream plasma, thus causing the SLAMS to become a part of and "reforming" the shock surface. In fact, it is thought that in the kinetic description, the quasi-parallel shock is made up of this reformation process. In MHD, on the other hand, the shock is simply a flow discontinuity (Schwartz and Burgess, 1991). Figure 1.3 shows a schematic of this process.

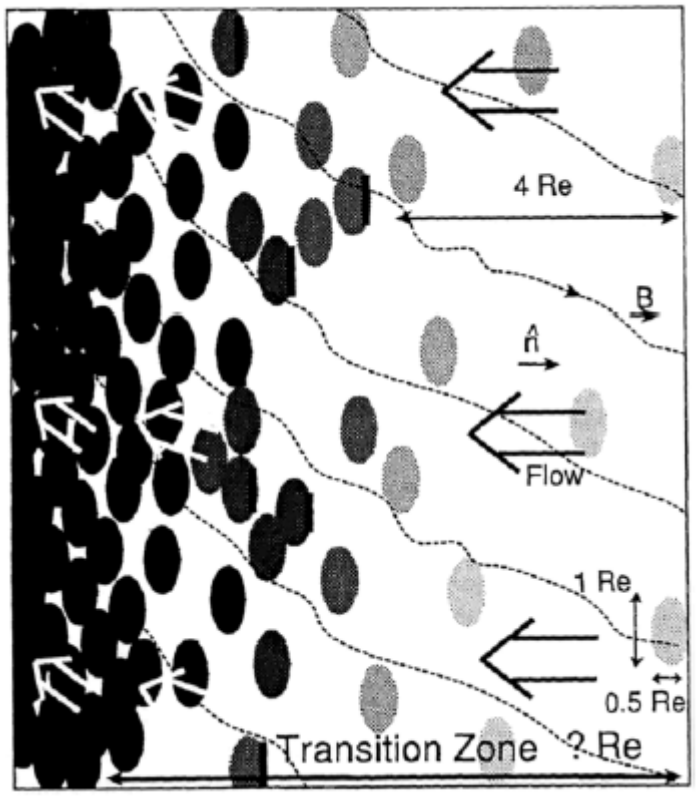

Figure 1.3: Schematic of SLAMS advecting into and reforming the bow shock. From Schwartz and Burgess (1991).

1.3 Magnetosheath Jets

1.3.1 Definitions

Magnetosheath jets are a class of phenomena marked by localised enhancements of dynamic pressure compared to the ambient magnetosheath. Jets, or at least a related phenomenon, were first described by Němeček et al. (1998). They used a definition based on proton flux and consequently called the phenomenon ”transient flux enhancement”, but since then many different terms and definitions have been developed and used. Savin et al. (2008) called their events ”high kinetic energy density plasma jets”, and defined them based on kinetic energy, as did Amata et al. (2011), who called them ”high kinetic energy jets”. Hietala et al. (2009) detected events of supermagnetosonic plasma flow within the magnetosheath and associated dynamic pressure enhancement that they called ”supermagnetosonic jets”. Karlsson et al. (2012) compared the magnetosheath plasma density to its time-average to detect transient enhancements, calling them ”plasmoids” and further dividing them into ”embedded plasmoids” that move at the magnetosheath velocity and ”fast plasmoids” that also show an enhancement in the anti-sunward velocity component. Archer and Horbury (2013) studied ”magnetosheath dynamic pressure enhancements” by comparing the magnetosheath dynamic pressure to its time-average to identify transient enhancements. Plaschke et al. (2013) compared the anti-sunward magnetosheath dynamic pressure to the solar wind dynamic pressure, calling the resulting observed enhancements ”high-speed jets”. Gunell et al. (2014) studied velocity enhancements in the magnetosheath, naming them ”plasmoids”. Dmitriev and Suvorova (2015) investigated enhancements of the total pressure compared to the solar wind, calling them ”large scale jets”. To avoid confusion and to keep the terminology as general as possible, we will henceforth call these phenomena ”magnetosheath jets”.

1.3.2 Occurrence and Properties

Several case studies and statistical studies have investigated where and under what conditions magnetosheath jets occur. Němeček et al. (1998) observed transient flux enhancements in the flank magnetosheath on streamlines connected to the quasi-parallel bow shock. Solar wind conditions were relatively steady, and the Alfvén Mach number $M_A = v/v_A$ was high. Savin et al. (2008) observed jets near the northern and southern cusps, downstream of the quasi-parallel bow shock, during relatively quiet solar wind conditions. Hietala et al. (2009, 2012) also observed jets downstream of the quasi-parallel bow shock. The large statistical study by Archer and Horbury (2013) found jets all over the dayside magnetosheath in the equatorial plane. Jets were more readily observed behind the quasi-parallel bow shock during steadier-than-normal IMF conditions. Low θ_{Bn} conditions were found to be more favourable for jet occurrence. According to Plaschke et al. (2013), the more or less only common feature of all jets is that they occur predominantly downstream of the quasi-parallel bow shock when the IMF cone angle, the angle between the IMF direction and the Sun-Earth line, is small.

The morphology and properties of magnetosheath jets have also been studied in both case studies and statistical studies of spacecraft observations. Němeček et al. (1998) found jets to have sizes in the direction parallel to the flow of 0.5-2.8 R_e. Savin et al. (2008) calculated the average flow-directional size of jets to be 1.3 R_e. Hietala et al. (2009, 2012) reported jet sizes perpendicular to the flow direction of 1-6 R_e. Karlsson et al. (2012, 2015) studied the morphology of plasmoids with regard to the magnetic field direction, finding fast plasmoids to be elongated in a direction approximately parallel to the magnetic field. Archer et al. (2012) and Archer and Horbury (2013) found jets to have sizes of 0.2-0.5 R_e perpendicular to the plasma flow and 1 R_e parallel to the flow, indicating an elongated shape. Plaschke et al. (2013, 2016) found jets to have flow-parallel sizes of around 0.71 R_e

and flow-perpendicular sizes of 1.34 R_e, indicating a pancake-like geometry.

Němeček et al. (1998) found jets to exhibit ion flux (density multiplied by velocity) enhancements of up to a factor of 5 compared to the background, corresponding to a dynamic pressure enhancement of 2-25 times the background. Savin et al. (2008) calculated dynamic pressure enhancements of 1.5-4 times the background magnetosheath level, with the contributions from density and velocity enhancement varying in their relation to each other. Hietala et al. (2009, 2012) found the dynamic pressure enhancement to be 6 times the background level and 2-7 times the solar wind level, with comparable contributions from enhancements of density and velocity. Karlsson et al. (2012, 2015) found enhancements in dynamic pressure to be > 1.5 times the background level, and they found different kinds of events, with the so-called "embedded plasmoids" showing an enhancement dominated by the contribution from density enhancement, and "fast plasmoids", which also show an enhancement in velocity. They found that a subset of plasmoids have a positive correlation between density enhancement and magnetic field enhancement, calling them "paramagnetic plasmoids". These also exhibit decreased perpendicular ion temperature compared to the surrounding magnetosheath. Archer et al. (2012) and Archer and Horbury (2013) found the dynamic pressure to be enhanced by a factor of 1.5-10 compared to the background magnetosheath, with the majority of jets being dominated by the contribution from velocity enhancement. Most of these jets are also associated with an increase in density, but for some there is a decrease in density. They also found that jets can be associated with an increase or decrease in magnetic field strength, but that density enhancements are correlated with increases in magnetic field strength. Increased density is also associated with decreased ion temperature, and vice versa. Plaschke et al. (2013, 2016) found the maximum dynamic pressure enhancement in jets to be 3-25 times the background magnetosheath levels, with the increase in velocity being 1-3 and the increase in density being 0.7-2 times

the background levels. Both increases and decreases in magnetic field strength were observed, with the maxima inside the jets corresponding to increases, similarly to the increases in density. They also found that jets exhibit decreases of both parallel and perpendicular temperatures, with the perpendicular decrease being significantly larger.

1.3.3 Jet formation mechanisms

Many theories have been proposed to explain the formation of magnetosheath jets. A solar wind rotational discontinuity impacting the bow shock transmits the discontinuity into the magnetosheath. Lin et al. (1996a,b) showed with 1D MHD and hybrid simulations that this results in the formation of pressure pulses in the magnetosheath, with the strongest pulses occurring where the shock geometry switches between quasi-parallel and quasi-perpendicular. Archer et al. (2012) found jets in spacecraft observations that are consistent with this mechanism, as they were preceded in time by the observation of discontinuities in the solar wind. Foreshock phenomena have been considered as a factor in jet formation since the first magnetosheath jet studies, with Nemecek et al 1998 reporting that jets were found downstream of the quasi-parallel bow shock. Hietala et al. (2009, 2012) proposed that rippling of the quasi-parallel bow shock could lead to the local shock geometry changing to quasi-perpendicular. According to the Rankine-Hugoniot conditions, the velocity component perpendicular to a shock normal does not decrease across the shock, allowing solar wind plasma to cross the bow shock without being significantly slowed down. This mechanism is illustrated in Figure 1.4. The dependence of the diversion of the flow at the shock on the shock normal angle is reminiscent of the refraction of a light ray at the interface between two media according to Snell's law. The RH conditions would still result in the plasma density increasing across the shock, leading to streams with dynamic pressures higher than the

ambient magnetosheath. Karlsson et al. (2015) studied the origin of paramagnetic plasmoids, finding that SLAMS impacting the bow shock where it is rippled could cause fast paramagnetic plasmoids, while SLAMS impacting a non-rippled part of the shock could be the origin of embedded plasmoids. Other formation mechanisms not necessarily linked to the foreshock have also been described.

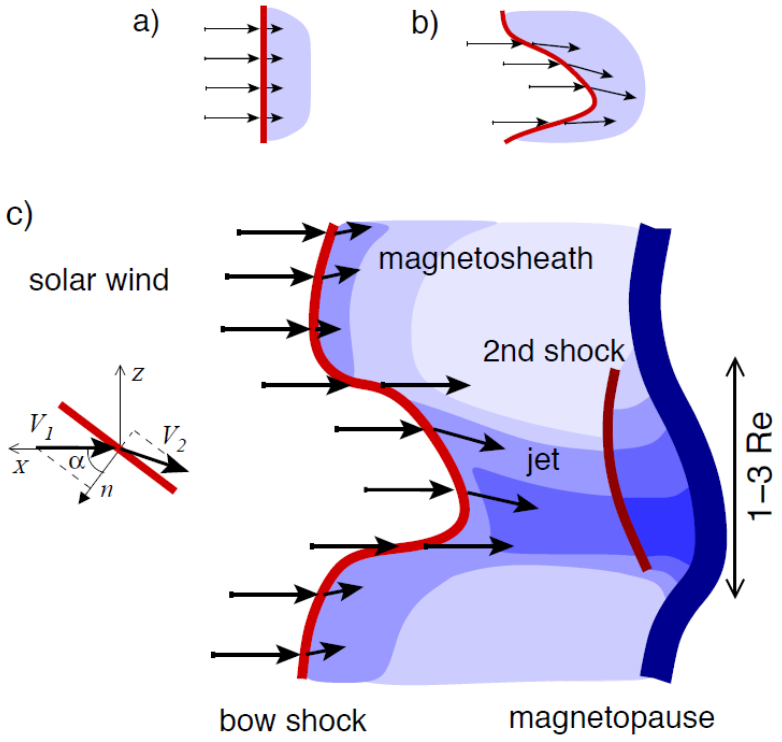

Figure 1.4: Diagram of the formation of magnetosheath jets through the bow shock ripple mechanism. X and Z are the GSE X- and Z-coordinate axes, V_1 indicates the upstream flow direction, V_2 indicates the downstream flow direction, n is the bow shock normal vector, and α is the angle between V_1 and n. In panel a, the upstream flow is parallel to the shock normal, $\alpha = 0$, so the flow is slowed down according to the Rankine-Hugoniot jumpt conditions across the shock. In panel b, the bow shock is rippled, and the flow is locally almost perpendicular to the shock normal, $\alpha \approx 90°$, and so the flow is not slowed down as much across the shock. Panel c shows that in the places where α is oblique, the flow is also deflected across the shock. Combined with the smaller slowdown across the shock, the ripple focuses the flow into a magnetosheath jet. From Hietala et al. (2012).

1.4 Outline of this thesis

This thesis is based on 3 papers. Palmroth et al. (2018b) is a case study of a magnetosheath jet identified in the global-hybrid simulation Vlasiator. The properties and evolution of this jet were studied, and the jet was found to be associated with the interaction between a SLAMS and the quasi-parallel bow shock. The study also found that jets can form during steady solar wind conditions. My contribution to this paper consisted of making some of the figures. Palmroth et al. (2021) conducted a statistical study of magnetosheath jets in Vlasiator and compared their properties with those of jets observed by the Magnetospheric Multiscale Mission (MMS) spacecraft formation. They found general agreement between simulation jets and observed jets, and also found that the properties of jets depend on the solar wind Alfvén Mach number M_A. For this paper, my task was to develop the algorithms for identifying, separating and tracking jets in Vlasiator, conducting the statistical analysis of jets in Vlasiator, as well as making the figures. The third paper, which is currently under preparation, concerns the research question of this thesis. In this paper, the method used in the statistical study Palmroth et al. (2021) is modified and extended to also perform a statistical analysis of foreshock compressive structures. For this paper, I have made the modifications to the algorithms, conducted the statistical analysis, and created all the figures, as well as done the majority of the writing.

The aim of this thesis is to investigate the link between foreshock phenomena and magnetosheath jets. The Methods chapter begins with a brief description of space plasma modeling frameworks by means of simulations, after which the simulation and simulation runs used in this study are introduced. Then, the criteria used to identify magnetosheath jets, foreshock compressive structures, and the different relevant regions of near-Earth space are defined. Finally, the algorithms for separating and tracking jets and foreshock compressive structures are explained.

In the Results chapter, statistical methods are utilised to determine select properties of foreshock compressive structures and magnetosheath jets. Then, magnetosheath jets are separated into two types, FCS-associated and non-FCS-associated, and the FCS criterion is varied. The occurrence rate of FCS-associated jets as a function of the variable FCS criterion is used to study the relationship between foreshock compressive structures and jets in the different simulation runs. The difference in magnetosheath penetration depth between the two types of jets is then briefly investigated. Finally, the formation of one particular non-FCS-associated jet is studied through visual inspection.

The Discussion chapter begins with a short summary of the results. After this, the FCS and jet properties as well as the jet occurrence rates are compared to literature. Next, the FCS hypothesis for jet formation is compared to similar theories in literature. Finally, the the strengths and weaknesses of using simulations to study foreshock structures and magnetosheath jets are discussed.

In the Summary and Conclusions chapter, a summary of the thesis is first presented. Finally, future prospects of studying foreshock structures and magnetosheath jets using Vlasiator as well as spacecraft observations are discussed.

2. Methods

2.1 Global Space Plasma Simulations

Plasma is a state of matter where the fraction of ionised particles in a gaseous medium is high enough that the behaviour of the matter is dominated by long-range electromagnetic interactions. Plasma is quasi-neutral, which means that the numbers of positive charges and negative charges are equal.

Modelling space plasmas is notoriously cumbersome, and modelling the interaction between the Interplanetary Magnetic Field (IMF), the Solar Wind (SW) and Earth's magnetic field is particularly difficult. In this section, the most important numerical approaches to plasma modelling will be introduced.

2.1.1 Numerical Plasma Descriptions

As mentioned in the introduction, one of the ways to model a plasma is to consider it a magnetised fluid. This magnetohydrodynamic (MHD) approach models only the bulk properties of the plasma such as density, bulk velocity, and thermal pressure. The time evolution of these bulk properties depend on themselves and each other as well as the electromagnetic fields in a set of continuity equations

$$\frac{\partial q}{\partial t} + \nabla \cdot \mathbf{F} = \sigma \tag{2.1}$$

where q is a bulk plasma property, $\mathbf{F}$ is the flux of q, and σ is the rate of creation or destruction of q. The interdependence of the electromagnetic fields and their time

evolution are governed by Maxwell's equations

$$\nabla \cdot \mathbf{E} = \frac{\rho_q}{\epsilon_0} \tag{2.2}$$

$$\nabla \cdot \mathbf{B} = 0 \tag{2.3}$$

$$\nabla \times \mathbf{E} = -\frac{\partial \mathbf{B}}{\partial t} \tag{2.4}$$

$$\nabla \times \mathbf{B} = \mu_0 \left(\mathbf{J} + \epsilon_0 \frac{\partial \mathbf{E}}{\partial t} \right) \tag{2.5}$$

where $\mathbf{E}$ is the electric field, ρ_q is the charge density, ϵ_0 is the vacuum permittivity, $\mathbf{B}$ is the magnetic flux density, μ_0 is the vacuum permeability, and $\mathbf{J}$ is the electric current. In MHD, quasi-neutrality means that $\rho_q = 0$. The displacement current $\frac{\partial \mathbf{E}}{\partial t}$ is also often neglected. To couple the electric and magnetic fields, an additional equation known as the generalised Ohm's law is required:

$$\mathbf{E} + \mathbf{V} \times \mathbf{B} = \frac{\mathbf{J}}{\sigma} + \frac{1}{qn_e}\mathbf{J} \times \mathbf{B} + \frac{1}{qn_e}\nabla \cdot \mathcal{P}_e + \frac{m_e}{q^2 n_e}\frac{\partial \mathbf{J}}{\partial t} \tag{2.6}$$

where $\mathbf{V}$ is the bulk velocity, σ is now the electrical conductivity, q is the ion charge, n_e is electron density, $\mathcal{P}_e$ is the electron pressure tensor, and m_e is the electron mass. In so called ideal MHD, Ohm's law reduces to

$$\mathbf{E} + \mathbf{V} \times \mathbf{B} = 0. \tag{2.7}$$

Together, the bulk plasma continuity equations, Maxwell's equations, and Ohm's law form the MHD equations. A problem arises, however, in the bulk plasma continuity equations specifically: For N continuity equations, we end up requiring $N+1$ variables, and so there is no closed-form solution to the equations. This problem is solved by providing a closure to the MHD equations. One common choice is coupling the thermal pressure and mass density through an equation of state $P\rho_m^\gamma = \text{constant}$, where P is the thermal pressure ρ_m is mass density, and γ is the polytropic index. The MHD equations have no analytical solutions except in trivial situations, so numerical simulations where the spatial domain is divided into elements of finite

volume, or cells, are required. Because the plasma is described only by its bulk properties in each cell, however, the computational costs of running a simulation are relatively modest for modern computers. As mentioned in the introduction, this comes at the cost of not being able to model kinetic effects.

To properly model kinetic effects, the plasma must be considered as something more complex than a bulk fluid. The microphysical approach considers the particles making up the plasma individually, each particle with mass m and charge q having a position $\mathbf{r}$ and a velocity $\mathbf{v}$, and an acceleration resulting from the Lorentz force

$$m\frac{d\mathbf{v}}{dt} = q(\mathbf{E} + \mathbf{v} \times \mathbf{B}). \tag{2.8}$$

For a large number of particles, numerical modeling of a plasma this way becomes completely intractable. However, by considering the positions and velocities as coordinates $(\mathbf{r}, \mathbf{v})$ in 6-dimensional phase space, one can define a distribution function $f(\mathbf{r}, \mathbf{v}, t)$ that takes values equal to the number N of particles with coordinates $(\mathbf{r}, \mathbf{v})$ at time t. This is called the kinetic plasma model. Particles of different species s can be gathered into separate distribution functions. If collisions between particles in the plasma can be neglected, which is the case for collisionless plasmas, the time evolution of the distribution function obeys the Vlasov equation

$$\frac{\partial}{\partial t} f_s(\mathbf{r}, \mathbf{v}, t) + \mathbf{v} \cdot \frac{\partial}{\partial \mathbf{r}} f_s(\mathbf{r}, \mathbf{v}, t) + \frac{q_s}{m_s}(\mathbf{E} + \mathbf{v} \times \mathbf{B}) \cdot \frac{\partial}{\partial \mathbf{v}} f_s(\mathbf{r}, \mathbf{v}, t) = 0 \tag{2.9}$$

where subscript s denotes the particle species in question. The electromagnetic fields again obey Maxwell's equations, and the generalised Ohm's law couples the electric field to the magnetic field. The distribution function contains all the information about the particles making up the plasma, but to derive the same bulk properties as in MHD, the velocity moments

$$\mu_k = \int \mathbf{v}^k f(\mathbf{r}, \mathbf{v}, t) d\mathbf{v} \tag{2.10}$$

of the distribution function must be calculated, with the 0th moment ($k = 0$) giving the number density $n(\mathbf{r}, t)$, the 1st moment giving the bulk velocity $\mathbf{U}(\mathbf{r}, t)$ in the

form of the number flux $n\mathbf{U}$, the 2nd moment giving the pressure tensor $\mathcal{P}(\mathbf{r}, \mathbf{t})$, and so on. Taking the velocity moments of the Vlasov equation, on the other hand, returns the MHD equations. The reason for the lack of kinetic effects in the MHD model is thus that velocity space is averaged and represented by a single temperature. In contrast, the kinetic model is theoretically an exact description of the plasma, though the paths of individual particles cannot be traced through space and time. This comes at the price of much higher computational cost, however. Both the spatial domain and velocity space must be divided into cells, and the time evolution of the distribution function must be solved in all of these cells. Also, because the plasma consists of at least protons and electrons, a minimum of two different particle species must be modeled. In practice, fully kinetic simulations require supercomputers, but even then concessions must be made in terms of the extents and resolutions of the spatial domain and velocity space, which affects the exactness of the plasma description.

However, there is no need to strictly choose between a single fluid MHD model and a fully kinetic model. The idea behind so called hybrid models is to mix and match different models. Multi-fluid models are based on the idea of treating different particle species (i.e. protons and electrons and possibly other ions) as separate fluids. This allows for the model to capture more complex physics. For instance, in this case, the divergence of the electric field need not be 0 as the densities of the different species are not necessarily equal. Recalling that depending on the closure used in the MHD model, the number of MHD equations can be different, the different fluids in a multi-fluid model need not be described by the same number of equations. One can also mix kinetic models and MHD, producing so called hybrid-Vlasov models, in which some species are described by distribution functions, while others are described by fluids (possibly with different numbers of MHD equations). The purpose of hybrid models is to allow more choice when it comes to how exact

one wants the model to be and how expensive one wants the computation to be. In hybrid-Vlasov models, for instance, computational costs are reduced at the price of not being able to resolve kinetic effects in some particle species.

Finally, one more way of modelling plasma numerically should be mentioned. Starting from the microphysical approach, one can choose to group particles close to each other in space into "macroparticles" instead of constructing distribution functions. This reduces the number of entities for which positions, velocities and Lorentz forces must be calculated, making numerical simulations using this model more tractable. The electromagnetic fields are still solved on a spatial grid of cells, based on which this model has acquired the name particle-in-cell (PIC). Increasing the size of the macroparticles, i.e. grouping more and more particles together, reduces computation costs, but this once again comes at the price of making the physics less exact.

2.1.2 Vlasiator

Vlasiator (Palmroth et al., 2018a) is a hybrid-Vlasov simulation. Protons, and potentially other ions, are modeled as distribution functions. The electrons, on the other hand, are treated as a fluid that preserves the quasi-neutrality of the plasma. The electromagnetic fields obey Maxwell's equations with the Darwin approximation of Ampère's law. In order to make the electromagnetic fields evolve with time as a function of the distribution functions, the system of equations is closed with the Hall MHD Ohm's law.

Vlasiator is inherently 6-dimensional, with 3 real space dimensions and 3 velocity space dimensions. The coordinate system of real space has Earth at the origin, the positive X-direction toward the Sun along the Earth-Sun line, the positive Z-direction toward ecliptic North, and the Y-axis completes the right-handed system (see Figure 1.1). The spaces are discretised into cubic cells arranged on an

Table 2.1: Properties of the different runs used in the study. From left to right, the columns give the run identifier, IMF vector (x,y,z), IMF strength, SW number density, SW velocity vector (x,y,z), IMF cone angle, and SW Alfvén Mach number. For all runs, the SW temperature is 0.5MK, the real space resolution is 227 km, and the velocity space resolution is 30 kms^{-1}.

Run	IMF [nT]	|IMF|	n [cm^{-3}]	v [kms^{-1}]	Cone angle [°]	M_A
HM30	(-4.3,2.5,0.0)	5	1	(-750,0,0)	30	6.9
HM05	(-5.0,0.4,0.0)	5	3.3	(-600,0,0)	5	10
LM30	(-8.7,5.0,0.0)	10	1	(-750,0,0)	30	3.4
LM05	(-10.0,0.9,0.0)	10	3.3	(-600,0,0)	5	5

evenly-spaced Cartesian grid. Each real space cell has a full set of velocity space cells associated with it, in which the VDF data for that real space cell is stored. The bulk plasma properties for the real space cell in question are calculated by taking the moments of the VDF. Each cell has a unique Cell ID, from which its position on its respective grid can be deduced.

Though Vlasiator is built to be 6D, the 4 simulation runs used in this study are all effectively 2D in real space, being restricted to 1-cell thick layer in the ecliptic plane (XY-plane). The different runs do not all have identical simulation boxes, but in all cases the box is large enough to capture the solar wind, the foreshock, the dayside magnetosheath, and part of the nightside. The boundary cells at the +X edge of the simulation box are set to have constant VDFs defined by the solar wind parameters (Table 2.1). At the -X and ±Y edges of the box, inflow boundary conditions are used. At the ±Z edges, periodic boundary conditions are used. The magnetic field in the simulation box is initialised as a combination of the IMF parameters (Table 2.1) and a magnetic dipole centered on Earth. In order to screen the source of the dipole and to avoid simulating the innermost magnetosphere where the timestep becomes very small due to the large magnetic field, an inner boundary consisting of a perfectly-conducting sphere with a radius of 5 R_e is placed around

the origin. The simulations runs presented in Table 2.1 are named according to whether they have higher Mach number (HM) or lower Mach number (LM), and whether the cone angle is 30° (30) or 5° (05).

The output data used in this study consisted of the bulk plasma properties for all real space cells, which was written approximately (due to variable time stepping) every 0.5 s of simulation time. Output velocity space data was also available for certain real space cells at certain times for some of the runs, but this data was not used in the study.

2.2 Jet and FCS Criteria

While magnetosheath jets are generally defined as being events of enhanced dynamic pressure in the magnetosheath, there is no single universally agreed-upon set of criteria to identify them. Plaschke et al. (2013) identify high-speed jets with time-intervals during which one of the THEMIS spacecraft observe a GSE X-directional dynamic pressure that is continuously at least 0.25 times the solar wind dynamic pressure as measured by the OMNI spacecraft at the same time (corrected for travel time), $P_{dyn,x} \geq 0.25 P_{dyn,sw}$, and has a peak of at least 0.5 times the SW dynamic pressure, $\max(P_{dyn,x}) \geq 0.5 P_{dyn,sw}$. Archer and Horbury (2013) also used THEMIS observations, but instead of comparing the dynamic pressure to the solar wind, they defined an ambient magnetosheath dynamic pressure by taking a 20-minute running time average of the THEMIS dynamic pressure data and required jets (which they called dynamic pressure enhancements) to have a dynamic pressure more than twice the ambient value, $P_{dyn} > 2 \langle P_{dyn} \rangle_{20min}$. Karlsson et al. (2012) used an approach similar to Archer & Horbury, but focusing on density enhancement instead of dynamic pressure. They defined density enhancements as time-intervals when the electron density as measured by one of the Cluster spacecraft was at least 1.5 times the ambient density, which was calculated as a 500-second running time average of

the density data from Cluster, $n > 1.5 \langle n \rangle_{500s}$.

The adaptation of these three criteria for Vlasiator data was studied by Palmroth et al. (2018b). For subsequent studies of jets in Vlasiator including this one, only the Archer & Horbury criterion was used. The Karlsson criterion, being based on density instead of dynamic pressure, identifies structures that may or may not be associated with enhancement of dynamic pressure, and so it was not used. The Plaschke criterion, on the other hand, does identify dynamic pressure enhancements, but as these are compared to the solar wind dynamic pressure, it also captures the entire solar wind as well as the acceleration regions at the flanks of the magnetosheath. Furthermore, we use here the Archer & Horbury criterion with a 3-minute time average instead of 20 minutes due to the limited durations of the simulation runs, $P_{dyn} > 2 \langle P_{dyn} \rangle_{3min}$. This criterion was found to be suitable by Palmroth et al. (2018b), and it was also used in Palmroth et al. (2021).

In order to study possible origins of jets in the foreshock, we introduce the concept of foreshock compressive structures, or FCSs for short. We define FCSs as structures in the foreshock where the ratio of magnetic field strength to IMF strength exceeds a particular threshold value, which we call the magnetic condition, $|\mathbf{B}| > \eta |\mathbf{B}_{IMF}|$. This condition can be varied so that differences between stronger (larger magnetic field enhancement) and weaker (smaller magnetic field enhancement) structures can be studied. Additionally, we require the structures to also have a dynamic pressure of at least 1.2 times the dynamic pressure of the pristine solar wind, which we call the compressive condition, $P_{dyn} \geq 1.2 P_{dyn,sw}$. This is done to prevent the magnetic condition from defining most of the bow shock region as a single, large FCS due to the ramping-up of the magnetic field strength across the shock.

Finally, we define the boundary between upstream and the magnetosheath in three different ways, as in Battarbee et al. (2020). The boundary defined by the

core heating criterion is the isocontour where the temperature of the core population of the plasma as defined in Wilson et al. (2014) is equal to 3 times the solar wind temperature, $T_{core} = 3T_{sw}$. The boundary defined by the magnetosonic Mach criterion is the isocontour where the x-directional magnetosonic mach number is equal to 1, $M_{ms,x} = v_x/\sqrt{v_A^2 + c_s^2} = 1$ where v_x is the velocity in the GSE X-direction, v_A is the Alfvén velocity, and $c_s = \sqrt{\gamma k_B T/m}$ is the sound speed, γ is the polytropic index, k_B is Boltzmann's constant, T is the temperature, and m is particle mass. The boundary defined by the density criterion is the isocontour where the density is equal to 2 times the solar wind density, $n = 2n_{sw}$.

2.3 Jet and FCS identification and tracking

The method described here was developed for the Palmroth et al. (2021) study. The jet identification and tracking algorithm begins with restricting the region where jets are searched for to a subset of the simulation box, so as to focus on the regions of space relevant to jet formation, propagation and dissipation. In practice, this means the foreshock, the subsolar and quasi-parallel magnetosheath, and the magnetopause. The inclusion of the foreshock also ensures that the search box can be used to identify FCSs. Searching for jets is also not performed over the entire simulation duration. Due to the nature of the simulation, it takes ∼200 seconds of simulation time from the beginning of the simulation to properly form the magnetosheath, bow shock, and foreshock. Because the Archer & Horbury criterion uses a 180 second running time average of the dynamic pressure, the search for jets is started at t=290 seconds in each simulation run. The jet search duration varies between runs, however, due to the different simulation durations. Again due to the jet criterion being used, jet search is stopped approximately 90 seconds before the end of the simulation. The specific search box boundaries and search durations for each simulation run can be found in Table 2.2. FCS search is performed using the

Table 2.2: The different parameters used in the FCS and jet tracking algorithm for each run: Search box (x_{min},x_{max},y_{min},y_{max}), jet tracking duration, and total number of jets found in the run. The "HM" runs have IMF magnitudes of 5 nT (corresponding to higher Alfvén Mach number), while the "LM" runs have IMF magnitudes of 10 nT (lower Mach number). The "30" runs have IMF cone angles of 30°, while the "05" runs have cone angles of 5°.

Run	Search box [R_e]	Tracking duration [s]	Number of jets
HM30	(6,18,-8,6)	129.5	128
HM05	(6,18,-6,6)	299.5	273
LM30	(6,18,-8,6)	379.5	380
LM05	(6,18,-6,6)	149.5	177

same search boxes and search durations.

For each time step in the output data (output cadence ∼0.5 s) in the jet search time interval, all the cells in the search box that fulfill the jet criterion are selected. Then, to further limit the search to only the magnetosheath, the cells where the core temperature is below 3 times the solar wind temperature are deselected. The resulting selection of cells for a particular output time step in run HM05 can be seen surrounded by the green contours in Figure 2.1. The orange curve in Figure 2.1 shows the boundary between foreshock and magnetosheath as defined by the core heating criterion. The IDs of the remaining selected cells are saved in an auxiliary file to be used in the subsequent steps of the algorithm. For the FCSs, all cells fulfilling the FCS magnetic condition are first selected. Then, the cells not fulfilling the FCS compressive condition are deselected. Finally, to limit the search for FCSs to the solar wind and foreshock in particular, all cells where the core temperature is at least 3 times the solar wind temperature are deselected. The resulting selection can be seen as the yellow contours in Figure 2.1. The IDs of the remaining selected cells are then saved in a manner similar to the jets.

Next, for each time step the selected jet cells are separated into disjoint regions.

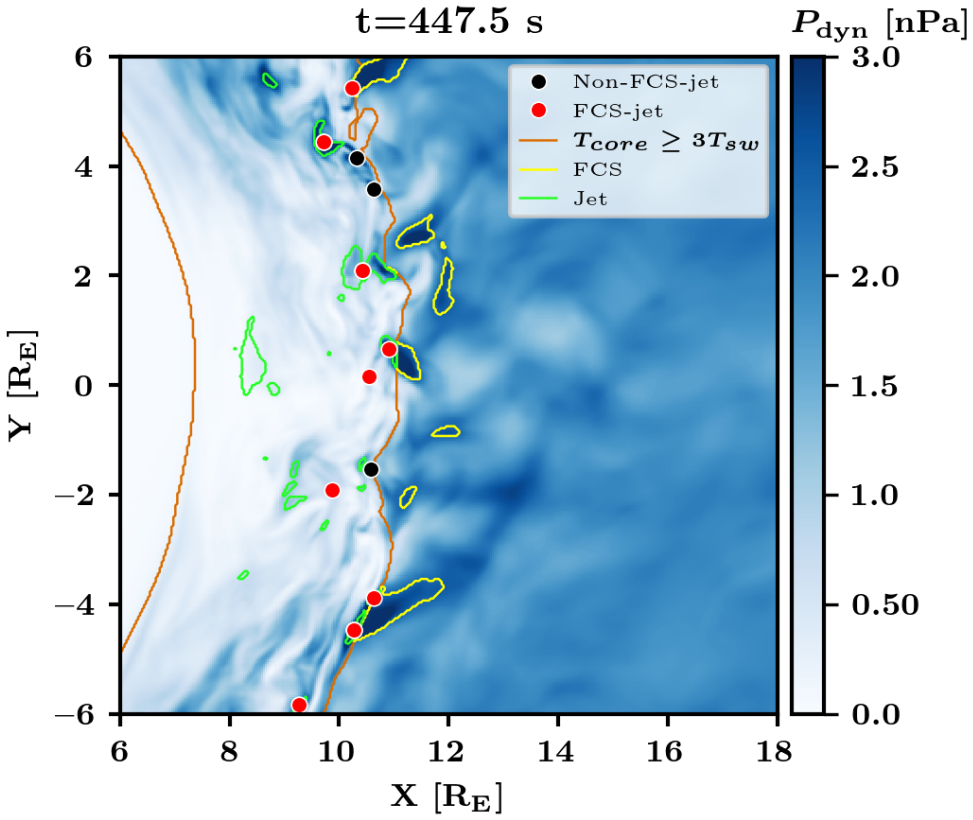

Figure 2.1: View of the subsolar magnetosheath and foreshock in run HM05 at 447.5 seconds from the start of the simulation with a FCS magnetic threshold of 1.5. The background colour shows the dynamic pressure. The orange contour delineates the region where the core heating criterion is fulfilled, the yellow contours delineate the regions where the FCS criteria are fulfilled, and the green contours delineate the regions where the jet criteria are fulfilled. The red dots mark the centers of jets that are, at any point in their lifetime, in contact with a region fulfilling the FCS criteria. The black dots mark the centers of jets that do not make contact with FCSs.

This is done by first taking a random selected cell (Figure 2.2b) and finding its neighbours. Recalling that the real space of the simulation is discretised into cubic cells arranged on a rectangular grid, the neighbours of a cell are defined as all the cells contained in the 5x5-cell square centered on the original cell, including the original cell itself (Figure 2.2c).[1] The neighbouring cells that are not selected as jet cells are discarded (Figure 2.2d), and then the neighbours of the remaining selected neighbours are found in the same way (Figure 2.2e,f). This process is repeated until no more selected neighbours are found, at which point the region is deemed fully identified, and the set of cell IDs making up the region are saved and stored for subsequent steps in the algorithm. Then, the process is begun anew, starting with a random selected cell that does not already belong to a fully identified region, repeating the process until all disjoint regions have been fully identified. For the FCSs, the process is the same, using the selecteded FCS cells for each time step to produce sets of disjoint FCS regions.

To track the disjoint jet regions over time, the cells making up the regions at two consecutive time steps are compared. If a disjoint region at $t = t_i$ and a disjoint region at $t = t_{i+1}$ overlap by at least 50% of the cells of the smaller of the two regions, then they are considered part of the same jet, and the jet is given a unique identifier if it doesn't already have one. This process is then performed for all the time steps in the tracking interval, producing a data set containing the time evolution of each jet in the tracking interval. The process is the same for the FCSs, using the disjoint FCS regions.

It is, of course, possible that one or multiple disjoint regions at t_i overlap with one or multiple regions at t_{i+1}. To account for this, the metadata tags "splinter" and "merger" are used. If a disjoint region at $t = t_i$ overlaps with multiple regions

[1] The cells at distance 2 along the axes are included to coarsen the resolution at which regions are separated, hopefully reducing the impact of possible effects caused by the simulation resolution.

at t_{i+1}, the largest of the regions (in terms of number of cells) is chosen as the successor of the original jet and is tracked normally, while for the smaller ones, their histories are copied from the original jet, but they are given new unique IDs and the tag "splinter". At future time steps, these new splinter jets are tracked normally. If multiple disjoint regions at t_i overlap with one region at t_{i+1}, the region that belongs to the oldest jet (in terms of the first time step at which the jet exists) is chosen as the originator and is tracked normally, while the regions associated with the younger jets are given the tag "merger". They are also tracked normally at future time steps. For the FCSs, the handling of splinters and mergers is the same as for jets. As a consequence of these rules, there may exist at certain time steps multiple jets/FCSs with different unique IDs that are currently associated with the same disjoint region and have either the same history or the same future path. This will be accounted for in the statistical analysis.

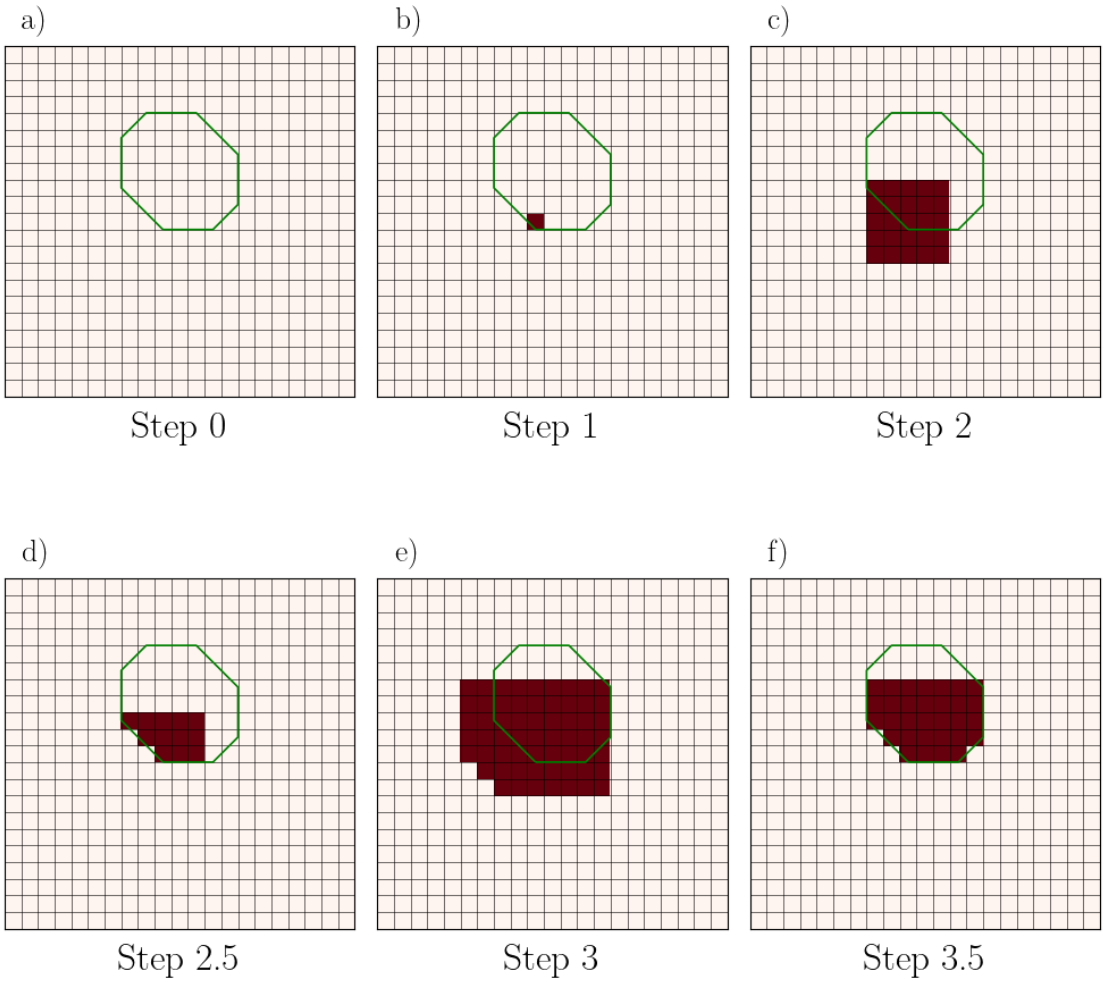

Figure 2.2: Diagram of the jet separation algorithm. Regions fulfilling the jet criteria are outlined in green, containing selected cells. Cells used by the separation algorithm to build up the individual jet are marked as dark red. In step 0 (panel a), the cells fulfilling the jet criteria has been identified and selected. In step 1 (panel b), a random selected cell is chosen. In step 2 (panel c), the neighbours of the cell are found. In step 2.5 (panel d), the neighbour cells that do not fulfill the jet criteria are discarded. In step 3 (panel e), the neighbours of the remaining neighbour cells are found. In step 3.5 (panel f), the neighbour cells that do not fulfill the jet criteria are discarded. Steps 3 and 3.5 are repeated until all the selected cells making up the individual jet have been found.

3. Results

For the statistical analysis, we are primarily interested in the jets that originate at the bow shock. A jet is defined to be at the bow shock if at least one of the cells making up the jet is at a distance of at most 2 cells from the upstream-magnetosheath boundary as defined by either the core heating criterion or the magnetosonic Mach criterion. For a jet to originate at the bow shock, this condition must be fulfilled at the time when the jet first forms. We discard from the statistical analysis all jets that do not originate at the bow shock. This is done because there are regions in the magnetosheath unrelated to jets that occasionally fulfill the jet criteria, probably due to the behaviour of local parameters. This was discussed in Palmroth et al. (2021).

The inclusion of all FCSs and jets in the statistical analysis regardless of whether they are splinters, mergers, both, or neither would give greater weight to FCSs and jets that produce many splinters or are the product of many mergers. To mitigate this effect, we discard jet splinters if the splintering happens after the jet has detached from the bow shock. Only the largest successor is retained. We also discard FCS mergers if the merge happens before the FCS reaches the bow shock. Only the oldest originator is retained. This way the relationship between FCS and jets can be studied while focusing on the formation of individual jets at the bow shock and the individual FCSs that interact with the bow shock.

3.1 Characterising FCSs

For the statistical analysis of FCS properties, the FCSs identified for a magnetic threshold of 1.5 in each run were collected into a single data set. The properties for each FCS were read at random times in the FCS' lifetime. This was done to make the results more comparable to possible spacecraft observations, because spacecraft have no control over which point in a transient structure's lifetime the structure is observed. Figure 3.1 shows the distributions of select FCS properties, with the histograms normalised by the total number of FCSs across all runs. Δn is calculated by subtracting from the maximum density within the FCS the average density of a two-cell-thick shell surrounding the FCS. This quantity is then normalised by the solar wind density n_{sw}. Only cells that belong to the upstream as defined by either the core heating or $M_{ms,x}$ criterion are included in the shell. $\Delta|v|$, ΔP_{dyn} and $\Delta|B|$ are calculated similarly, using the velocity magnitude, dynamic pressure and magnetic field strength respectively, normalised by their respective solar wind values. For ΔT, the average temperature of the shell is subtracted from the average temperature of the FCS, and the quantity is then normalised by the solar wind temperature. The lifetime is calculated by subtracting the first point in time when the FCS is tracked from the last point in time when it is tracked. The tangential size is calculated by dividing the total area of the cells making up the FCS by the radial size of the jet, which is defined as the x-directional distance between the cell within the FCS with the smallest x-coordinate and the cell with the largest x-coordinate. The size ratio is calculated by dividing the radial size by the tangential size.

The FCS density is generally enhanced compared to the surrounding plasma, ranging from almost no enhancement to over one solar wind density unit. In contrast, the velocity is nearly the same as for the surroundings. The dynamic pressure is thus generally enhanced, ranging from almost the same as the surrounding plasma to over one solar wind dynamic pressure unit. The magnetic field strength is enhanced

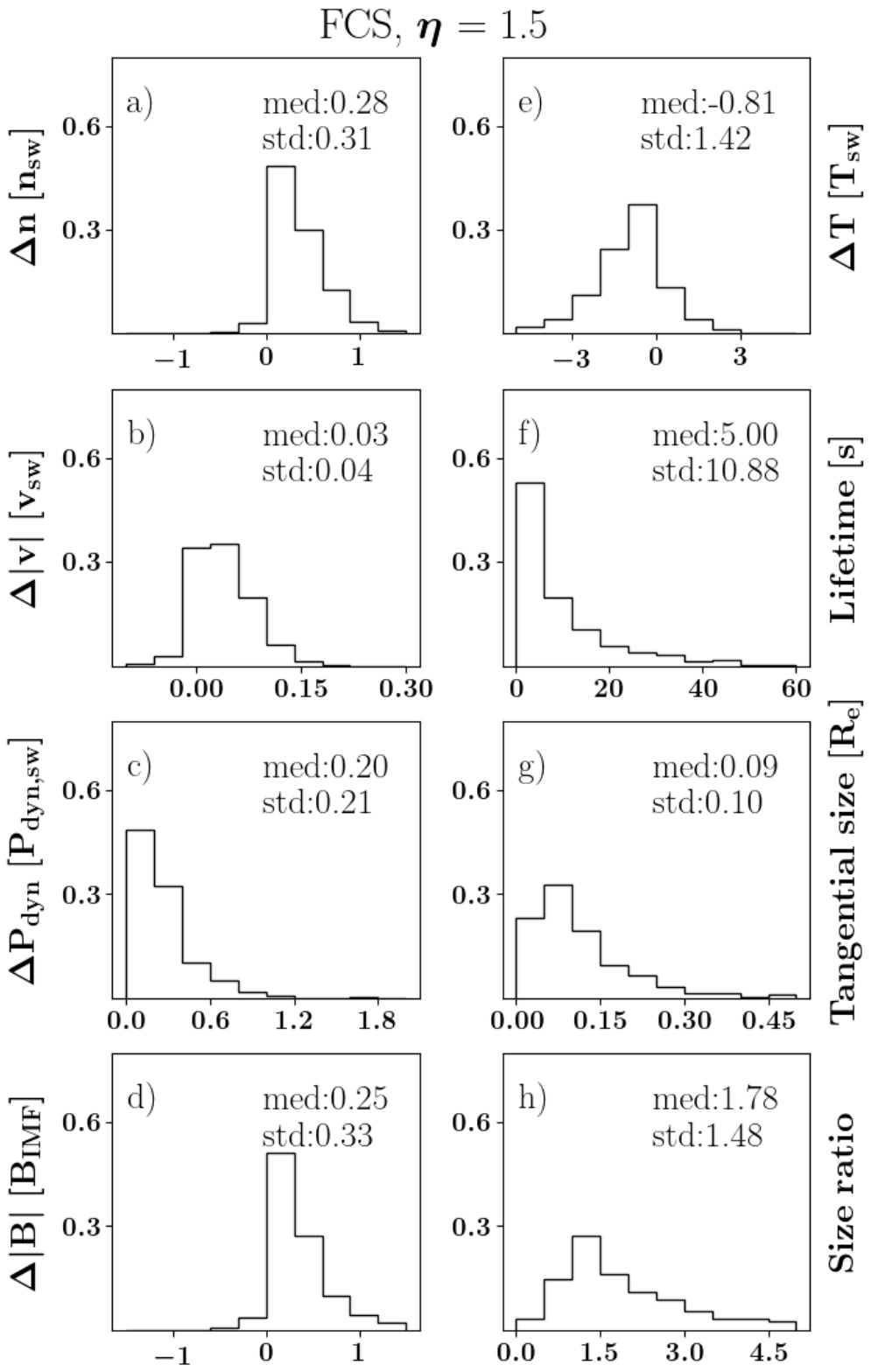

Figure 3.1: Select statistically calculated properties of FCSs for a magnetic threshold of 1.5: Enhancements of a) density, b) velocity magnitude, c) dynamic pressure, d) magnetic field strength magnitude, and e) temperature compared to surrounding plasma and normalised by the solar wind values, as well as distributions of FCS f) lifetimes, g) tangential sizes, and h) size ratios.

very similarly to the density, ranging from almost no enhancement to over 1 IMF field strength unit. For a small fraction of FCSs the average temperature is higher than the surrounding plasma, but for the majority the temperature is lower. The decrease ranges from almost none to over 3 times the solar wind temperature. The FCSs have lifetimes ranging from a few seconds to almost a minute. Their tangential sizes are mostly around 0.1 R_e, with a small number reaching over 0.3 R_e. The size ratios are generally significantly larger than 1, indicating that FCSs are elongated in the plasma flow direction, with a calculated median radial size of 0.179 R_e.

3.2 Characterising jets

The jet properties are acquired using the same method as for the FCSs. Characterising jets in this manner was first done by Palmroth et al. (2021) for the purpose of comparing jet in Vlasiator to jets observed by the MMS spacecrafts. Figure 3.2 shows the properties of the jets. For the jets, only cells belonging to the downstream (defined by the complement of the criteria used for the upstream in the case of FCSs) are included in the shell used for the Δ calculations. The Δ quantities are again normalised by their corresponding solar wind values. The jet density is generally enhanced over the surrounding plasma, but a significant fraction of jets show a density decrease instead. The difference in density ranges from around -2 to 4 solar wind density units. The velocity, on the other hand, is almost always enhanced, ranging from very little enhancement to over 0.3 times the solar wind speed. The dynamic pressure is also enhanced, with the enhancement ranging from above 0 to over 1.8 solar wind dynamic pressure units. The magnetic field strength is also generally enhanced, but like the density, a significant fraction of jets show a decrease in magnetic field strength. The difference to the surrounding plasma ranges from around -1.5 to over 1.5 IMF field strength units. Some jets show a higher temperature than the surroundings, but for the majority the temperature is

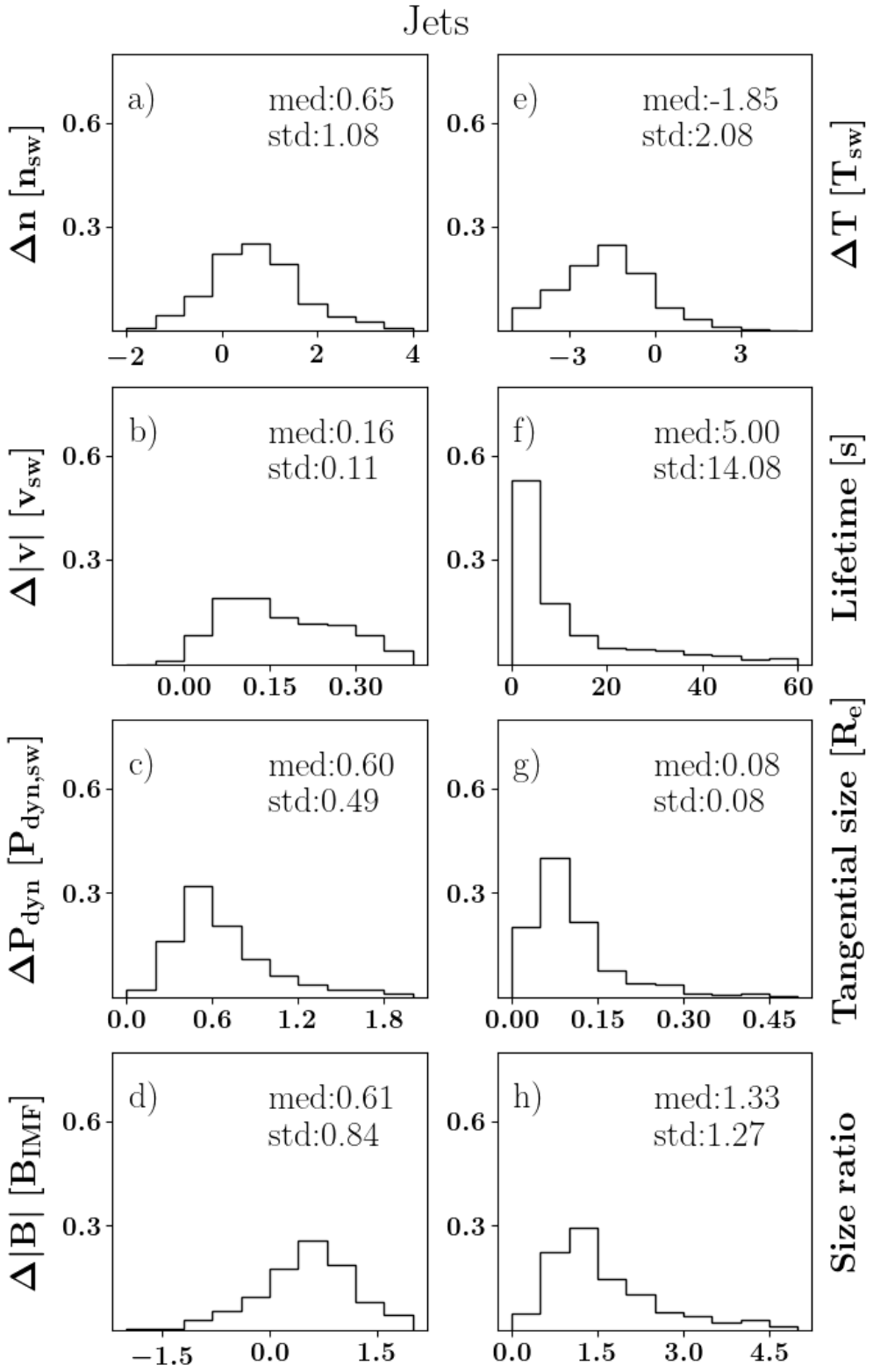

Figure 3.2: Select statistically calculated properties of magnetosheath jets: Enhancements of a) density, b) velocity magnitude, c) dynamic pressure, d) magnetic field strength magnitude, and e) temperature compared to surrounding plasma and normalised by the solar wind values, as well as distributions of jet f) lifetimes, g) tangential sizes, and h) size ratios.

lower, up to over 4 solar wind temperature units lower. The jets' lifetimes range from a few seconds to around a minute, similarly to the FCSs. Their tangential sizes are mostly around 0.1 R_e like the FCSs, but with a slightly smaller median and a thinner tail toward the large sizes. Like the FCSs, most jets have a size ratio above 1 and are thus elongated in the x-direction. The jet size ratio tail is thinner than for the FCSs.

3.3 Formation of jets

In order to study the influence of FCSs on jets, we further separate the jets used in the statistical analysis into two categories based on whether they form near FCSs or not. A jet where at least one of the constituent cells are at a distance of at most 2 cells from an FCS at any point in its lifetime is categorised as an "FCS-jet". The rest of jets are categorised as "non-FCS-jets". The separation of jets into these two categories can be seen in Figure 2.1.

By varying the FCS magnetic threshold, the effect of the amplitude of the FCS magnetic field enhancement on jet formation can be studied. We produced data sets according to the FCS and jet definition, identification and tracking methods for various FCS magnetic thresholds between 1.1 and 3.0, separately for each different simulation run. For each data set, the number of jets, number of FCS-jets and number of FCSs were counted. Figure 3.3 shows quantities derived from these numbers as a function of the FCS magnetic threshold. Figure 3.3a shows the FCS occurrence rate, defined as the total number of FCSs identified divided by the tracking duration (see Table 2.2) for the different simulations runs. The black curve corresponds to run HM30, blue to HM05, green to LM30, and orange to LM05. The FCS occurrence rate is the average rate at which new FCSs appear. At low values of the magnetic threshold, the occurrence rate is similar for all runs except LM05. This is because LM05 is a low-Mach run and the foreshock structures are

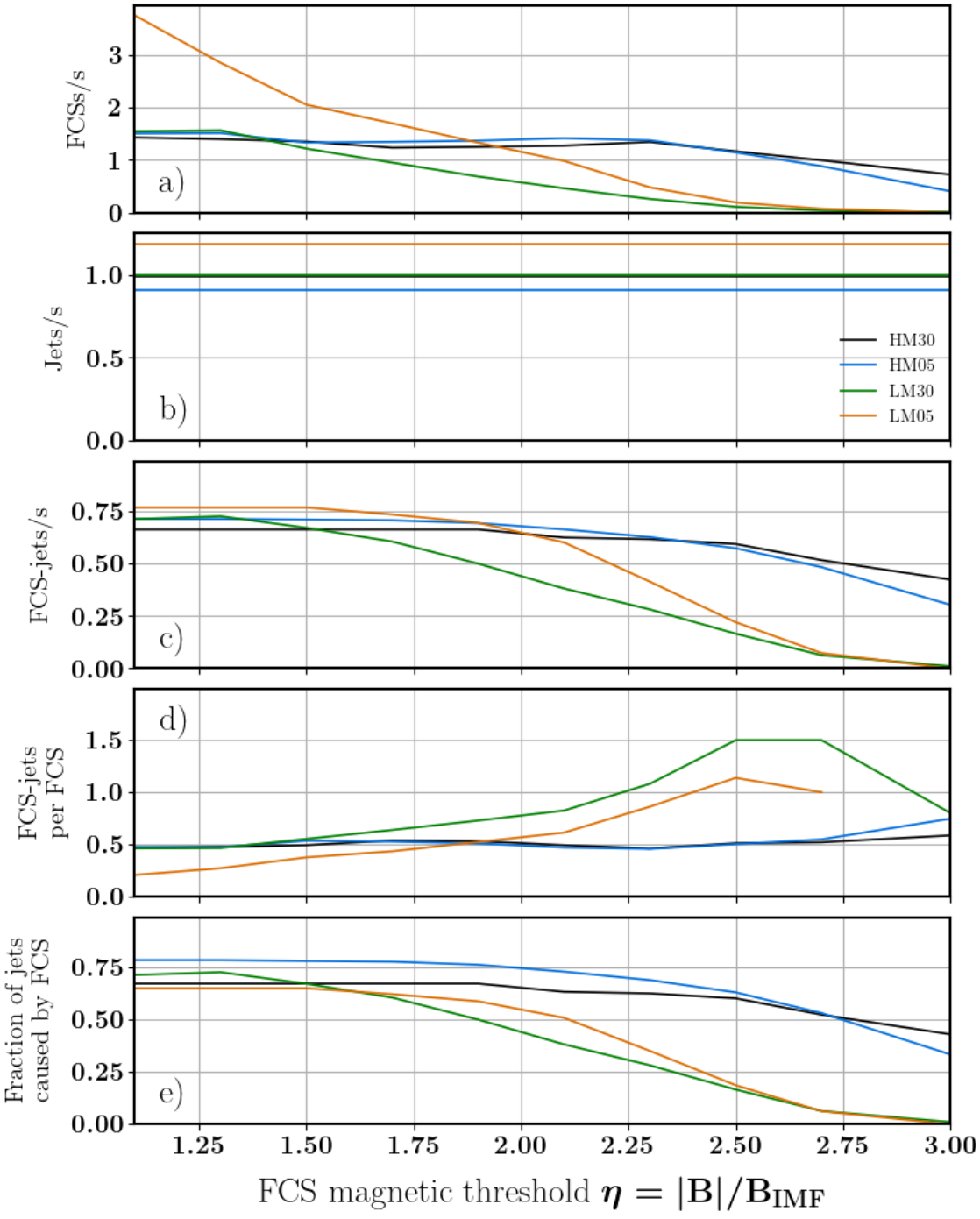

Figure 3.3: Dependence of jet and FCS statistics on FCS magnetic threshold for the 4 different simulation runs: a) FCS occurrence rate, b) jet occurrence rate, c) FCS-jet occurrence rate, d) ratio of FCS-jets to FCSs, and e) fraction of jets caused by FCSs. The black curves correspond to run HM30, the blue curves to HM05, green to LM30, and orange to LM05. The occurrence rates measure the average rate at which new structures (FCSs, jets, or FCS-jets) appear.

small Turc et al. (2018). Together with the search box capturing a very large portion of the entire foreshock (as compared to LM30), this means that more FCSs fit in the box simultaneously, yielding a higher occurrence rate. At higher values of the magnetic threshold, the FCS occurrence rate decreases more quickly for the low-Mach runs, indicating that the structures in those runs have lower amplitudes, and that increasing the magnetic threshold results in less FCSs. Figure 3.3b shows the jet occurrence rate, defined as the total number of jets identified divided by the tracking duration. These values are constant over the entire range of the magnetic thresholds. This is expected, as the jet criteria do not depend on the FCS magnetic threshold. There are no clearly significant differences between the different runs when it comes to jet occurrence. Figure 3.3c shows the FCS-jet occurrence rate, defined as the total number of FCS-jets identified divided by the tracking duration. For low values of the magnetic threshold, the FCS-jet occurrence rate is very similar across the runs, corresponding to 75% of the jet occurrence rate. At higher values, the rate decreases more quickly for the low-Mach runs. This is again expected, as the FCS-jet occurrence rate is correlated with the FCS occurrence rate, so a lack of FCSs in the upstream results in a lack of FCS-jets. Figure 3.3d shows the ratio of FCS-jets to FCSs, defined by dividing the total number of identified FCS-jets by the total number of identified FCSs. This ratio is close to constant across the entire magnetic threshold range for the high-Mach runs, but for the low-Mach runs, there is significant change for larger magnetic thresholds. At the lower end of the range, the high occurrence rate of FCSs in run LM05 causes the ratio to be lower than for the other runs. At the higher end of the range, the low total number of FCSs identified in the low-Mach runs leads to more variation. For the high-Mach runs, the ratio of FCS-jets to FCSs is almost a constant 0.5, while in the low-Mach runs the few but strong FCSs are associated with the formation of more than 1 FCS-jet per FCS. For run LM05, the ratio cannot even be calculated for a magnetic

threshold of 3.0, as no FCSs (and consequently no FCS-jets) are identified at this value of the threshold. Figure 3.3e shows the fraction of jets associated with FCSs, defined as the total number of identified FCS-jets divided by the total number of identified jets. For low magnetic threshold values, this fraction is quite similar across the runs, around 75%. For run LM30, the fraction remains approximately constant until a magnetic threshold of ~ 1.3 after which it starts decreasing noticeably. For runs HM30, HM05, and LM05, the fraction remains approximately constant until a magnetic threshold of ~ 2, after which it starts decreasing noticeably.

Figure 3.4 shows how far FCS-jets and non-FCS-jets travel downstream from the bow shock. The distance from the bow shock of a jet is defined as the x-directional distance between the center of the jet and a 5th degree polynomial fit to the locations of the cells closest to the bow shock as defined by the core heating criterion. In Figure 3.4a, the bow shock-jet distance is taken for every jet at the last time in the lifetime of the jet. These distances are then accumulated to make the histogram, with the accumulation normalised by the tracking duration of the run each jet belongs to. Finally, the accumulation is averaged over the 4 runs, giving the average disappearance rate of jets at different distances from the bow shock. Most of the FCS-jets and non-FCS-jets disappear close to the bow shock. Farther downstream of the bow shock, there are virtually no non-FCS-jets left, but FCS-jets are still observed. Figure 3.4b is accumulated similarly, but with the accumulation normalised by the number of jets of each type in each run instead of the tracking duration. The histogram is also made cumulative. This essentially gives the average probability of a jet of given type to penetrate the magnetosheath to at least a given distance from the bow shock. FCS-jets are seen to penetrate deeper into the magnetosheath than non-FCS-jets, with FCS-jets having an e-folding distance of 0.43 R_e, twice that of non-FCS-jets.

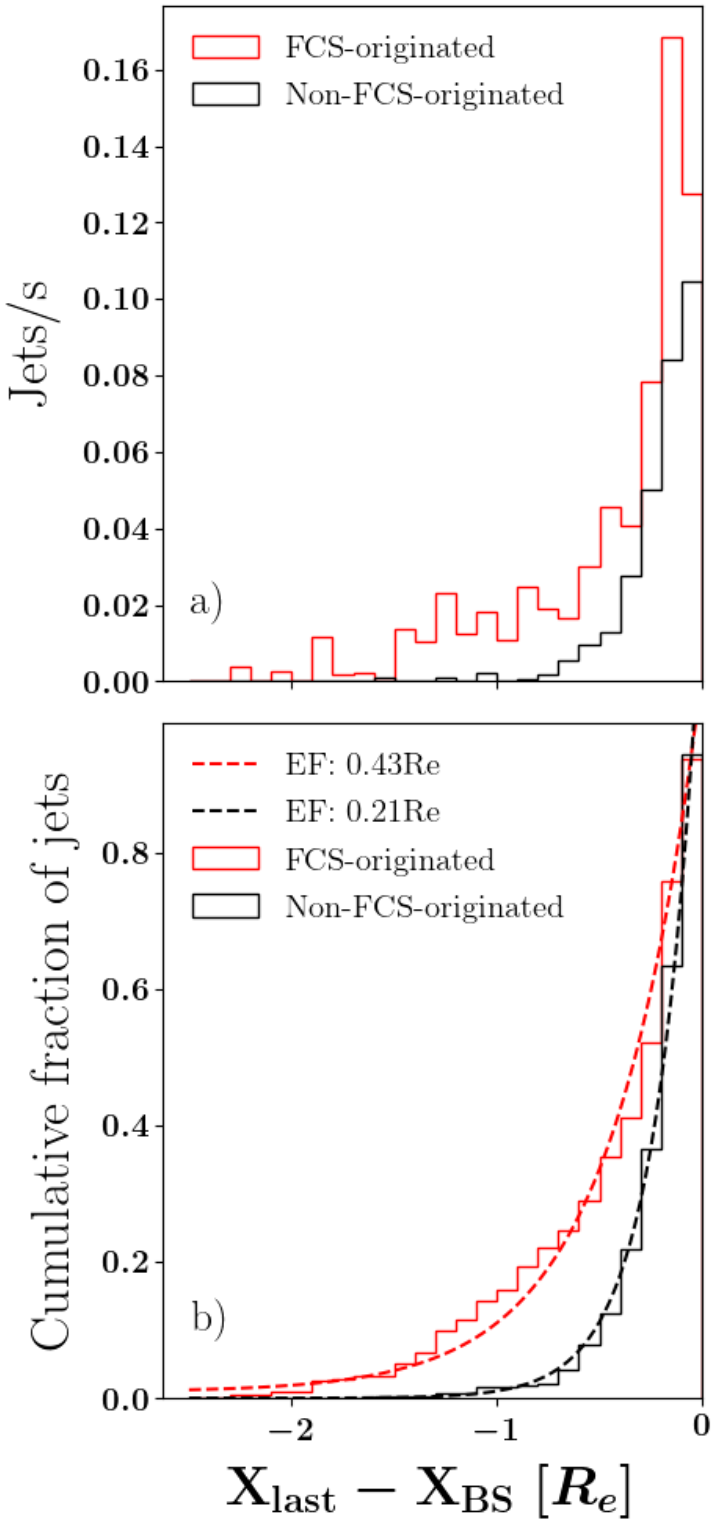

Figure 3.4: Histograms of jet location downstream of the bow shock with FCS magnetic threshold 1.5: a) Number of jets per second disappearing at different depths in the magnetosheath, and b) probability of jets to penetrate to a particular depth in the magnetosheath.

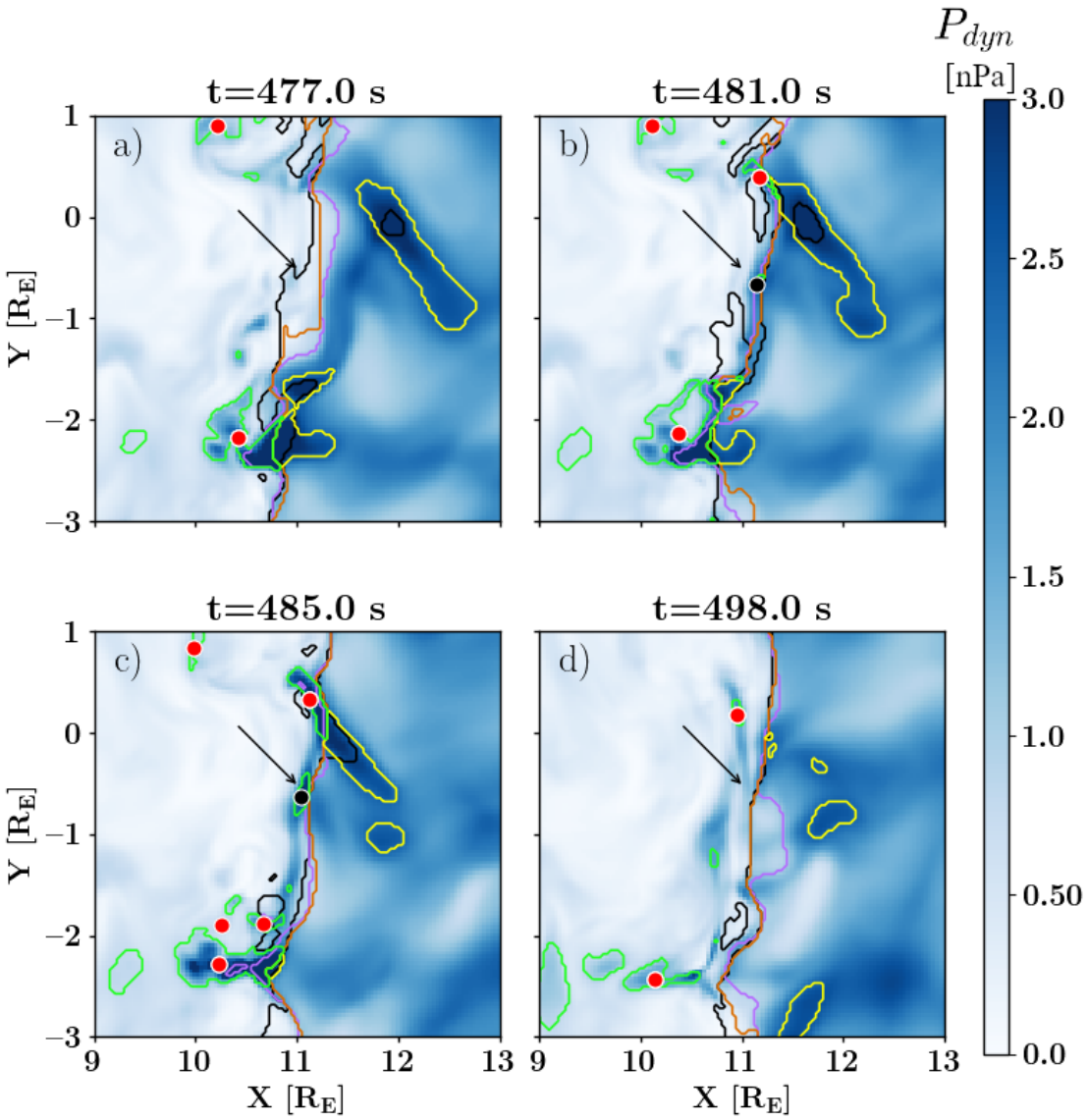

Figure 3.5: Views of run HM05 at a) 477.0, b) 481.5, c) 485.0, and d) 498.0 seconds from the start of the simulation, investigating the formation of the non-FCS jet at (11.25,-0.6) R_E in panel b. Contours and dots as in Figure 1, with 2 additional contours: The $M_{MS,x}$ criterion (violet) and the density criterion (black).

The formation mechanism of non-FCS-jets remains unclear. Figure 3.5 shows the formation, evolution and disappearance of a single non-FCS-jet in run HM05. Figure 3.5a shows the magnetosheath, bow shock and foreshock shortly before the jet begins to form at the location indicated by the black arrow. At this point in time, there is a visible non-locality of the bow shock (Battarbee et al., 2020) with the density-based shock boundary being earthward of the $M_{ms,x}$- and core heating-based boundaries. Figure 3.5b shows the non-FCS-jet in question just as it is beginning to form. The bow shock behind it has reformed and is no longer non-local. In Figure 3.5c the non-FCS-jet has formed and evolved for a few seconds, and the shock behind it has not changed significantly. In Figure 3.5d the jet has disappeared, and the $M_{ms,x}$ boundary behind the indicated location has moved sunward, making the shock non-local again. In the figure, several FCS-jets can also be seen forming both duskward and dawnward of the non-FCS-jet. The bow shock appears to be at least slightly indented in front of incoming FCSs, with shock reformation happening as the FCSs contact the shock and the FCS-jets form.

4. Discussion

In this thesis, we have conducted a statistical study of the relationship between foreshock compressive structures and magnetosheath jets. We found that up to 75% of jets are associated with FCSs impacting the bow shock, and that these FCS-jets penetrate deeper into the magnetosheath than non-FCS-jets. No conclusive explanation was found for the formation mechanism of non-FCS-jets.

The median scale size of FCS identified for $\eta = 1.5$ is 0.09 R_e, which is approximately 573 km. This agrees somewhat well with the SLAMS coherence length scales of $\sim$ 1000 km reported by Lucek et al. (2002, 2004, 2008), as well as with the observed SLAMS scale sizes of $>\sim$ 600 km reported by Behlke et al. (2003) and $<$ 800 km reported by Schwartz et al. (1992). This is an interesting result, as the magnetic threshold $\eta = 1.5$ corresponds more closely to the magnetic field enhancements found in shocklets than those of SLAMS. A possible explanation for this is that the additional compressive criterion used in identifying FCS for this study cuts off a significant part of the structures if only part of the structures exhibit enhanced dynamic pressures high enough to fulfill the compressive criterion. As the bulk velocity in FCS is not significantly enhanced, the compressive criterion also means that there is a positive correlation between magnetic field enhancement and density enhancement. Behlke et al. (2003) also found such a positive correlation between the magnetic field enhancement and enhancement of the negative spacecraft potential, which is a proxy for the plasma density. We also found a significant median decrease

in the ion temperature inside FCS, which could explain the underheating of SLAMS at the bow shock reported by Schwartz et al. (1992).

Comparing the properties of magnetosheath jets identified in this study to the spacecraft observations of Archer and Horbury (2013), we find a median enhancement in both velocity and density, which agrees with the spacecraft observations that the majority of magnetosheath jets display both increased density and velocity with respect to the surrounding plasma. The spacecraft observations show that this subset of the magnetosheath jets tend to have enhanced magnetic field strength and lower temperature than the surrounding plasma, which agrees with the median increase in magnetic field strength and median decrease in temperature found in Vlasiator jets. It is also interesting to compare the results of this study to the results of Palmroth et al. (2021). The methods used in this study are a modified version of the methods used in the earlier study, but they are not identical. In this study, we require jets to form at the bow shock, the bow shock itself is slightly differently defined, we restrict the surrounding plasma of jets to only magnetosheath plasma, and we do not discard jets with lifetimes < 5 s. In light of these differences, the morphology and properties of the jets found in this study agree quantitatively with both the Vlasiator jets and the MMS jets found in Palmroth et al. (2021). Finally, we note that the properties of FCS and magnetosheath jets identified in this study are quite similar in that both show enhancements of magnetic field and density, and a decrease in temperature. This is similar to the findings of Karlsson et al. (2015), who noted the same similarities between SLAMS in the foreshock and paramagnetic plasmoids in the magnetosheath.

Magnetosheath jets have also been found in other simulations. Karimabadi et al. (2014) found jets with sizes of 2.4 and 0.3 R_e in the flow-parallel and flow-perpendicular directions respectively. The increase in dynamic pressure was 6 times the surrounding magnetosheath, and jets were associated with decreases in ion tem-

perature and increases in magnetic field strength. In the simulation by Hao et al. (2016), jets had sizes of 1 and 0.2 R_e parallel and perpendicular to the flow direction, respectively. The dynamic pressure increase was around 4 times the background magnetosheath level. The ion temperature was decreased, and magnetic field strength was increased. The spatial sizes reported by these studies correspond to jets that are both larger and more elongated than the median tangential sizes and size ratios of jets found in Vlasiator, which could be explained by the fact that we use the solar wind flow direction rather than the sheath flow direction as the parallel (radial) direction. Different jet criteria also result in different jet sizes. The other simulations appear to agree with Vlasiator regarding jets having enhanced magnetic field strength and cooler plasma.

The behaviour of the FCS occurrence rates as a function of the magnetic threshold (Figure 3.3a) is clearly different in the $B_{IMF} = 10$ nT runs (LM30,LM05) than the 5 nT runs (HM30,HM05). The larger occurrence rate of FCS at low η in run LM05 and faster drop-off with increasing η in runs LM30 and LM05 implies that the FCS are spatially smaller and exhibit smaller enhancements of magnetic field strength in the 10 nT runs. This is consistent with the findings by Turc et al. (2018) that the foreshock ULF waves have shorter wavelengths and exhibit smaller magnetic field fluctuations in 10 nT runs compared to 5 nT runs. The faster FCS occurrence rate drop-off for the 10 nT runs is also naturally reflected in the FCS-jet occurrence rates and fraction of jets caused by FCS (because the jet occurrence rate does not depend on η).

For the 5 nT runs, the FCS occurrence rate, and hence the FCS-jet occurrence rates and fraction of jets caused by FCS, drops off slowly with increasing η, consistent with the magnetic field fluctuations being larger than in the 10 nT runs. An interesting feature is the almost constant ratio ~ 0.5 of FCS-jets to FCS in the 5 nT runs. This implies that either multiple (~ 2) FCS are involved in the formation of

one jet, or that not all FCS cause jets. In the former scenario, it could be that as an FCS approaches the bow shock and slows down, another FCS behind it catches up and the two FCS merge. In the latter scenario, it could be that additional environmental conditions are required for the formation of jets from FCS. This would be consistent with Karlsson et al. (2015), who argued that SLAMS impacting the bow shock where it is indented could lead to the formation of paramagnetic plasmoids.

For all the simulation runs, the fraction of jets caused by FCSs asymptotically approaches ~ 0.75 as the magnetic threshold η is decreased, which means that up to 75% of magnetosheath jets are caused by FCSs. However, this also means that a minority of jets are not associated with even the weakest magnetic field enhancements in the foreshock. There appear to to be 2 points in the FCS magnetic threshold where the behaviour of the fraction of jets caused by FCSs change rather abruptly: $\eta \approx 1.3$ for run LM30 and $\eta \approx 2$ for runs HM30, HM05, and LM05. The former could correspond to the foreshock compressional boundary $\delta B/B_0 \approx 0.4$ between regions of low-amplitude and high-amplitude waves described by Rojas-Castillo et al. (2013). The latter corresponds to the smallest rms wave amplitudes $\delta B/B_0 \sim 1$ of SLAMS observed by Schwartz et al. (1992). $\eta \approx 2$ may then describe the transition from non-SLAMS structures to the weakest SLAMS.

The comparison of magnetosheath penetration depth between FCS-jets and non-FCS-jets (Figure 3.4) shows that FCS-jets can penetrate significantly deeper into the magnetosheath, implying that the two different jet types have different properties. The decrease of the disapperance rate of jets with increasing depth in the magnetosheath agrees with Plaschke et al. (2013, 2016), who found the observation rate of jets to be three times higher in the subsolar magnetosheath than near the magnetopause.

The non-FCS-jets could perhaps be associated with foreshock structures of enhanced magnetic field but ambient dynamic pressure, as these would not fulfill the

FCS compressive criterion. However, observing the formation of the non-FCS-jet indicated by the arrow in Figure 3.5b, we see that the dynamic pressure is enhanced on the upstream side of the bow shock. If this dynamic pressure enhancement is associated with decreased magnetic field strength, this would fit the theory by Karlsson et al. (2015) that diamagnetic plasmoids could be associated with diamagnetic structures, or magnetic holes, in the foreshock. Applying this theory to the results in this study requires diamagnetic plasmoids to make up a subset of magnetosheath jets as defined by the Archer and Horbury (2013) criterion.

Looking at the FCSs and FCS-jets in Figure 3.5 shows that FCSs approaching and impacting the bow shock appears to be associated with indentation, non-locality, and reformation of the shock. This supports the theory by Schwartz and Burgess (1991) that the quasi-parallel shock is a "patchwork of three-dimensional structures", continuously reforming due to incoming SLAMS. In our study, FCsS serve the role of the SLAMS. Based on this, we can say that treating the Earth's bow shock as a magnetohydrodynamic shock where the local angle between flow direction and shock normal determines whether magnetosheath jets can or cannot form is too oversimplified of a model. As up to 75% of jets are caused by FCS, kinetic effects should be considered when developing theories about the formation mechanisms of jets.

Recalling the trade-offs that must be made when selecting a model for numerically describing plasma, it should again be noted that the accurate modelling of ion kinetic effects in Vlasiator came at the cost of the simulation runs used in this study being 2D in real space. Limiting the simulation to the ecliptic plane specifically is not a big problem when comparing results with spacecraft observations, because these are also usually confined to approximately the ecliptic plane (or the polar plane). However, spacecraft observations still take place in 3D real space, where magnetic fields twist and turn in 3 dimensions and plasma flows around the

magnetosphere in 3 dimensions. 2D Vlasiator runs can only approximately model the true behaviour of near-Earth plasma and magnetic fields, and so-called "2D effects" arise in these simulation runs. For instance, the compression of plasma at the 2D bow shock leads to higher ion temperatures in the magnetosheath, and plasma tends to pile up in front of the magnetopause, causing the bow shock boundary to gradually move sunward over time. These effects do not prevent qualitative comparison between spacecraft observations and simulations, but they must be noted. Additionally, the lack of kinetic electrons in these Vlasiator runs means that any influence of electron kinetic effects on spacecraft observations cannot be reproduced in the simulations.

On the other hand, the global nature of the Vlasiator simulation runs also has significant strengths when it comes to studying transient structures such as FCS and magnetosheath jets. As shown in Palmroth et al. (2021) and this study, global simulations allow us to trace the paths of FCS and jets across time and space, determine their lifetimes, measure their sizes and shapes along any arbitrary axis in the simulation domain, as well as track the evolution of their properties over time. This can be done in the entire simulation domain at once, whereas spacecraft or spacecraft formations are restricted to a limited set of points in space at each point in time. Global simulations thus have both weaknesses and strengths when compared to spacecraft observations, but the strengths alone make them a very useful tool for studying the properties and dynamics of near-Earth space.

5. Summary and Conclusions

We studied the properties, occurrence, and relationship between foreshock compressive structures and magnetosheath jets. We found that, for an FCS magnetic threshold value of $\eta = 1.5$, FCSs have lifetimes on the order of seconds to tens of seconds, tangential sizes of around $0.1R_e$, and radial size-tangential size ratios of around 1-2. FCSs exhibit enhancements of density, dynamic pressure and magnetic field strength compared to the surrounding plasma. Velocity is not significantly enhanced, and the temperature is lower than for the surrounding plasma.

Jets also have lifetimes on the order of seconds to tens of seconds, tangential sizes of around $0.1R_e$, and slightly lower size ratios than FCSs. Jets exhibit enhancements of density, dynamic pressure, magnetic field strength, and velocity compared to the surrounding plasma, and also show a decrease in temperature.

Varying the FCS magnetic threshold η gives the occurrence rates of FCSs, jets, and FCS-jets as a function of the threshold. The occurrence rates of FCSs in the low-Mach number runs (LM30 and LM05) decrease more quickly with increasing η than in the high-Mach number runs (HM30 and HM05). The occurrence rates of FCS-jets behave similarly, as do the fractions of jets caused by FCS. At low to medium values of $\eta <\sim 2$, we find that up to 75% of jets are caused by FCS.

Comparing the magnetosheath penetration depths of FCS-jets and non-FCS-jets reveals that FCS-jets travel significantly deeper than non-FCS-jets. The e-folding distance of the fraction of FCS-jets that penetrate at least a certain distance

from the bow shock is over twice the rate for non-FCS-jets.

Visual inspection of the formation of a non-FCS-jet revealed bow shock non-locality but no significant indentation of the bow shock at the formation site. Bow shock reformation occurs around the same time and place as the formation of the non-FCS-jet, but it remains unclear if the jet formation is related to this.

We conclude that there is strong evidence for the theory that a majority of magnetosheath jets are caused by magnetic structures in the foreshock such as FCSs, supporting the conclusions of Karlsson et al. (2015) and Palmroth et al. (2018b, 2021), in contrast to the bow shock ripple theory put forth by Hietala et al. (2009, 2012). Not all jets are associated with FCSs, however. These non-FCS-jets appear to have short lifetimes and disappear quite close to the bow shock, while FCS-jets appear to live longer and penetrate deeper into the magnetosheath. Thus the two different types of jets may be associated with different formation mechanisms.

5.1 Future prospects and outlook

The methods used in this study are powerful in their capability of identifying, separating and tracking FCSs and jets and studying their properties and relationships during different solar wind conditions as a function of lifetime. However, the extent of the knowledge about FCSs and jets that can be obtained is limited by the simulation data used in the study. The real space domain of the simulation runs used in this study are restricted to the ecliptic plane, and thus we cannot yet say anything about FCSs and jets in regions not intersected by the ecliptic plane. This is also true for satellite spacecraft, which orbit the Earth in roughly a single plane, usually either the ecliptic or polar plane. The simulation runs also cover only 4 different sets of solar wind parameters, and we can only make educated guesses about different conditions based on the results we have.

5.1.1 Simulation studies

There is no lack of data that can be used for future studies, however. The Vlasiator simulation has been run in the polar plane as well, and so future studies can shine a light on the differences between FCSs and jets in the polar plane compared to the ecliptic plane. The code and algorithms used in this study can almost be used as-is for polar runs, only minor modifications to some assumptions are necessary. There is also some variety in the solar wind parameters used in the polar runs. A more detailed study of the formation of non-FCS-jets in both polar and ecliptic simulation runs could also be conducted.

Recently, Vlasiator simulation runs with full 3D real space domains have also been run successfully, and so studying FCSs and jets in the full foreshock and magnetosheath is now technically possible. However, the data format used for the 3D runs has some significant differences compared to the 2D runs, so extensive modifications must be made to the code and algorithms used in this study.

Finally, we recall that Vlasiator is a *hybrid*-Vlasov simulation. FCSs and jets are both associated with ion kinetic effects, but any possible influence of electron kinetic effects on them cannot currently be probed by Vlasiator. However, a version of Vlasiator that models electrons kinetically, eVlasiator, is currently under development. In the future, it may be possible to investigate the kinetic effects of electrons on the formation of jets.

5.1.2 Spacecraft studies

Statistical studies of magnetosheath jets observed by spacecraft have been conducted. Because one spacecraft can only be in one place at one time, these studies are essentially reliant on spacecraft crossing jets by chance. This is not a problem if jets occur frequently, the spacecraft's orbit is optimally chosen, and/or observations are collected over long periods of time. However, studying the relationship

between foreshock structures and magnetosheath jets based on spacecraft observations is more complicated. To observe an individual foreshock structure impacting the bow shock and forming a magnetosheath jet would require several spacecraft, each of them in their own right place at the right time. Finding such an event from current spacecraft observations would thus be quite a serendipitous discovery.

Planning a multiple spacecraft mission with orbits fine-tuned to increase the chance of observing jet formation from FCSs could, however, be possible in theory. Further simulation and spacecraft studies of magnetosheath jets and foreshock structures under different solar wind conditions could assist in fine-tuning the orbits.

Acknowledgements

The author acknowledges the European Research Council for Starting grant 200141-QuESpace, with which Vlasiator (http://helsinki.fi/vlasiator) was developed, and Consolidator grant Consolidator grant 682068-PRESTISSIMO, awarded to further develop Vlasiator and use it for scientific investigations. The author acknowledges the Academy of Finland for grant number 312351, which funds The Finnish Centre of Excellence in Research of Sustainable Space, which participates in supporting Vlasiator development and science. The author acknowledges the CSC-IT Center for Science in Finland for providing computing environments that made this study possible.

I would like to thank my supervisor and censor, prof. Minna Palmroth, and censor prof. Tomas Karlsson of the KTH Royal Institute of Technology in Stockholm, for their part in the process of preparing and evaluating this thesis. I thank my coworkers and colleagues at home and abroad for their expert advice and comments. I thank my friends for the emotional support they have provided throughout the research and writing process. Finally, I would like to thank my parents, Ilkka Suni and Ulrika Gyllenberg, for their unending and persistent encouragement.

Bibliography

E. Amata, S. P. Savin, D. Ambrosino, Y. V. Bogdanova, M. F. Marcucci, S. Romanov, and A. Skalsky. High kinetic energy density jets in the Earth's magnetosheath: A case study. *Planetary and Space Science*, 59(7):482–494, 2011. ISSN 0032-0633. doi: 10.1016/j.pss.2010.07.021.

M. O. Archer and T. S. Horbury. Magnetosheath dynamic pressure enhancements: Occurrence and typical properties. *Annales Geophysicae*, 31(2):319–331, 2013. ISSN 0992-7689. doi: 10.5194/angeo-31-319-2013.

M. O. Archer, T. S. Horbury, and J. P. Eastwood. Magnetosheath pressure pulses: Generation downstream of the bow shock from solar wind discontinuities. *Journal of Geophysical Research: Space Physics*, 117(A5), 2012. ISSN 2156-2202. doi: 10.1029/2011JA017468.

Markus Battarbee, Urs Ganse, Yann Pfau-Kempf, Lucile Turc, Thiago Brito, Maxime Grandin, Tuomas Koskela, and Minna Palmroth. Non-locality of Earth's quasi-parallel bow shock: Injection of thermal protons in a hybrid-Vlasov simulation. *Annales Geophysicae*, 38(3):625–643, 2020. ISSN 0992-7689. doi: 10.5194/angeo-38-625-2020.

Rico Behlke, Mats André, Stephan C. Buchert, Andris Vaivads, Anders I. Eriksson, Elizabeth A. Lucek, and Andre Balogh. Multi-point electric field measurements of Short Large-Amplitude Magnetic Structures (SLAMS) at the Earth's quasi-

parallel bow shock. *Geophysical Research Letters*, 30(4), 2003. ISSN 1944-8007. doi: 10.1029/2002GL015871.

A. V. Dmitriev and A. V. Suvorova. Large-scale jets in the magnetosheath and plasma penetration across the magnetopause: THEMIS observations. *Journal of Geophysical Research: Space Physics*, 120(6):4423–4437, 2015. ISSN 2169-9402. doi: 10.1002/2014JA020953.

J. W. Dungey. Interplanetary Magnetic Field and the Auroral Zones. *Physical Review Letters*, 6(2):47–48, 1961. doi: 10.1103/PhysRevLett.6.47.

J. P. Eastwood, E. A. Lucek, C. Mazelle, K. Meziane, Y. Narita, J. Pickett, and R. A. Treumann. The Foreshock. *Space Science Reviews*, 118(1):41–94, 2005. ISSN 1572-9672. doi: 10.1007/s11214-005-3824-3.

H. Gunell, G. Stenberg Wieser, M. Mella, R. Maggiolo, H. Nilsson, F. Darrouzet, M. Hamrin, T. Karlsson, N. Brenning, J. De Keyser, M. André, and I. Dandouras. Waves in high-speed plasmoids in the magnetosheath and at the magnetopause. *Annales Geophysicae*, 32(8):991–1009, 2014. ISSN 0992-7689. doi: 10.5194/angeo-32-991-2014.

Y. Hao, B. Lembege, Q. Lu, and F. Guo. Formation of downstream high-speed jets by a rippled nonstationary quasi-parallel shock: 2-D hybrid simulations. *Journal of Geophysical Research: Space Physics*, 121(3):2080–2094, 2016. ISSN 2169-9402. doi: 10.1002/2015JA021419.

H. Hietala, T. V. Laitinen, K. Andréeová, R. Vainio, A. Vaivads, M. Palmroth, T. I. Pulkkinen, H. E. J. Koskinen, E. A. Lucek, and H. Rème. Supermagnetosonic Jets behind a Collisionless Quasiparallel Shock. *Physical Review Letters*, 103(24): 245001, 2009. doi: 10.1103/PhysRevLett.103.245001.

H. Hietala, N. Partamies, T. V. Laitinen, L. B. N. Clausen, G. Facskó, A. Vaivads, H. E. J. Koskinen, I. Dandouras, H. Rème, and E. A. Lucek. Supermagnetosonic subsolar magnetosheath jets and their effects: From the solar wind to the ionospheric convection. *Annales Geophysicae*, 30(1):33–48, 2012. ISSN 0992-7689. doi: 10.5194/angeo-30-33-2012.

M. M. Hoppe, C. T. Russell, L. A. Frank, T. E. Eastman, and E. W. Greenstadt. Upstream hydromagnetic waves and their association with backstreaming ion populations: ISEE 1 and 2 observations. *Journal of Geophysical Research: Space Physics*, 86(A6):4471–4492, 1981. ISSN 2156-2202. doi: 10.1029/JA086iA06p04471.

H. Karimabadi, V. Roytershteyn, H. X. Vu, Y. A. Omelchenko, J. Scudder, W. Daughton, A. Dimmock, K. Nykyri, M. Wan, D. Sibeck, M. Tatineni, A. Majumdar, B. Loring, and B. Geveci. The link between shocks, turbulence, and magnetic reconnection in collisionless plasmas. *Physics of Plasmas*, 21(6):062308, 2014. ISSN 1070-664X. doi: 10.1063/1.4882875.

T. Karlsson, N. Brenning, H. Nilsson, J.-G. Trotignon, X. Vallières, and G. Facsko. Localized density enhancements in the magnetosheath: Three-dimensional morphology and possible importance for impulsive penetration. *Journal of Geophysical Research: Space Physics*, 117(A3), 2012. ISSN 2156-2202. doi: 10.1029/2011JA017059.

T. Karlsson, A. Kullen, E. Liljeblad, N. Brenning, H. Nilsson, H. Gunell, and M. Hamrin. On the origin of magnetosheath plasmoids and their relation to magnetosheath jets. *Journal of Geophysical Research: Space Physics*, 120(9): 7390–7403, 2015. ISSN 2169-9402. doi: 10.1002/2015JA021487.

Margaret G. Kivelson and Christopher T. Russell. Introduction to Space Physics. *Introduction to Space Physics, Edited by Margaret G. Kivelson and Christopher*

T. Russell, pp. 586. ISBN 0521451043. Cambridge, UK: Cambridge University Press, April 1995., 1995.

Hannu E. J. Koskinen. *Physics of Space Storms: From the Solar Surface to the Earth.* Springer-Verlag, 2011. ISBN 978-3-642-00319-6. doi: 10.1007/978-3-642-00319-6.

Y. Lin, L. C. Lee, and M. Yan. Generation of dynamic pressure pulses downstream of the bow shock by variations in the interplanetary magnetic field orientation. *Journal of Geophysical Research: Space Physics*, 101(A1):479–493, 1996a. ISSN 2156-2202. doi: 10.1029/95JA02985.

Y. Lin, D. W. Swift, and L. C. Lee. Simulation of pressure pulses in the bow shock and magnetosheath driven by variations in interplanetary magnetic field direction. *Journal of Geophysical Research: Space Physics*, 101(A12):27251–27269, 1996b. ISSN 2156-2202. doi: 10.1029/96JA02733.

E. A. Lucek, T. S. Horbury, M. W. Dunlop, P. J. Cargill, S. J. Schwartz, A. Balogh, P. Brown, C. Carr, K.-H. Fornacon, and E. Georgescu. Cluster magnetic field observations at a quasi-parallel bow shock. *Annales Geophysicae*, 20(11):1699–1710, 2002. ISSN 0992-7689. doi: 10.5194/angeo-20-1699-2002.

E. A. Lucek, T. S. Horbury, A. Balogh, I. Dandouras, and H. Rème. Cluster observations of structures at quasi-parallel bow shocks. *Annales Geophysicae*, 22(7): 2309–2313, 2004. ISSN 0992-7689. doi: 10.5194/angeo-22-2309-2004.

E. A. Lucek, T. S. Horbury, I. Dandouras, and H. Rème. Cluster observations of the Earth's quasi-parallel bow shock. *Journal of Geophysical Research: Space Physics*, 113(A7), 2008. ISSN 2156-2202. doi: 10.1029/2007JA012756.

J. G. Luhmann. The Solar Wind Interaction with Venus and Mars: Cometary Analogies and Contrasts. In *Cometary Plasma Processes*, pages 5–16. Ameri-

can Geophysical Union (AGU), 1991. ISBN 978-1-118-66366-0. doi: 10.1029/GM061p0005.

Z. Němeček, J. Šafránková, L. Přech, D. G. Sibeck, S. Kokubun, and T. Mukai. Transient flux enhancements in the magnetosheath. *Geophysical Research Letters*, 25(8):1273–1276, 1998. ISSN 1944-8007. doi: 10.1029/98GL50873.

Minna Palmroth, Urs Ganse, Yann Pfau-Kempf, Markus Battarbee, Lucile Turc, Thiago Brito, Maxime Grandin, Sanni Hoilijoki, Arto Sandroos, and Sebastian von Alfthan. Vlasov methods in space physics and astrophysics. *Living Reviews in Computational Astrophysics*, 4(1):1, 2018a. ISSN 2365-0524. doi: 10.1007/s41115-018-0003-2.

Minna Palmroth, Heli Hietala, Ferdinand Plaschke, Martin Archer, Tomas Karlsson, Xóchitl Blanco-Cano, David Sibeck, Primož Kajdič, Urs Ganse, Yann Pfau-Kempf, Markus Battarbee, and Lucile Turc. Magnetosheath jet properties and evolution as determined by a global hybrid-Vlasov simulation. *Annales Geophysicae*, 36(5):1171–1182, 2018b. ISSN 0992-7689. doi: 10.5194/angeo-36-1171-2018.

Minna Palmroth, Savvas Raptis, Jonas Suni, Tomas Karlsson, Lucile Turc, Andreas Johlander, Urs Ganse, Yann Pfau-Kempf, Xochitl Blanco-Cano, Mojtaba Akhavan-Tafti, Markus Battarbee, Maxime Dubart, Maxime Grandin, Vertti Tarvus, and Adnane Osmane. Magnetosheath jet evolution as a function of lifetime: Global hybrid-Vlasov simulations compared to MMS observations. *Annales Geophysicae*, 39(2):289–308, 2021. ISSN 0992-7689. doi: 10.5194/angeo-39-289-2021.

E. N. Parker. Dynamics of the Interplanetary Gas and Magnetic Fields. *The Astrophysical Journal*, 128:664, 1958. ISSN 0004-637X. doi: 10.1086/146579.

F. Plaschke, H. Hietala, and V. Angelopoulos. Anti-sunward high-speed jets in the

subsolar magnetosheath. *Annales Geophysicae*, 31(10):1877–1889, 2013. ISSN 0992-7689. doi: 10.5194/angeo-31-1877-2013.

F. Plaschke, H. Hietala, V. Angelopoulos, and R. Nakamura. Geoeffective jets impacting the magnetopause are very common. *Journal of Geophysical Research: Space Physics*, 121(4):3240–3253, 2016. ISSN 2169-9402. doi: 10.1002/2016JA022534.

D. Rojas-Castillo, X. Blanco-Cano, P. Kajdič, and N. Omidi. Foreshock compressional boundaries observed by Cluster. *Journal of Geophysical Research: Space Physics*, 118(2):698–715, 2013. ISSN 2169-9402. doi: 10.1029/2011JA017385.

S. Savin, E. Amata, L. Zelenyi, V. Budaev, G. Consolini, R. Treumann, E. Lucek, J. Safrankova, Z. Nemecek, Y. Khotyaintsev, M. Andre, J. Buechner, H. Alleyne, P. Song, J. Blecki, J. L. Rauch, S. Romanov, S. Klimov, and A. Skalsky. High energy jets in the Earth's magnetosheath: Implications for plasma dynamics and anomalous transport. *JETP Letters*, 87(11):593–599, 2008. ISSN 1090-6487. doi: 10.1134/S0021364008110015.

Steven J. Schwartz. Magnetic field structures and related phenomena at quasi-parallel shocks. *Advances in Space Research*, 11(9):231–240, 1991. ISSN 0273-1177. doi: 10.1016/0273-1177(91)90039-M.

Steven J. Schwartz and David Burgess. Quasi-parallel shocks: A patchwork of three-dimensional structures. *Geophysical Research Letters*, 18(3):373–376, 1991. ISSN 1944-8007. doi: 10.1029/91GL00138.

Steven J. Schwartz, David Burgess, William P. Wilkinson, Ramona L. Kessel, Malcolm Dunlop, and Herman Luehr. Observations of short large-amplitude magnetic structures at a quasi-parallel shock. *Journal of Geophysical Research*, 97:4209–4227, 1992. ISSN 0148-0227. doi: 10.1029/91JA02581.

John R. Spreiter and Stephen S. Stahara. A new predictive model for determining solar wind-terrestrial planet interactions. *Journal of Geophysical Research: Space Physics*, 85(A12):6769–6777, 1980. ISSN 2156-2202. doi: 10.1029/JA085iA12p06769.

M. F. Thomsen, S. J. Schwartz, and J. T. Gosling. Observational evidence on the origin of ions upstream of the Earth's bow shock. *Journal of Geophysical Research: Space Physics*, 88(A10):7843–7852, 1983. ISSN 2156-2202. doi: 10.1029/JA088iA10p07843.

L. Turc, U. Ganse, Y. Pfau-Kempf, S. Hoilijoki, M. Battarbee, L. Juusola, R. Jarvinen, T. Brito, M. Grandin, and M. Palmroth. Foreshock Properties at Typical and Enhanced Interplanetary Magnetic Field Strengths: Results From Hybrid-Vlasov Simulations. *Journal of Geophysical Research: Space Physics*, 123(7):5476–5493, 2018. ISSN 2169-9402. doi: 10.1029/2018JA025466.

L. B. Wilson, D. G. Sibeck, A. W. Breneman, O. Le Contel, C. Cully, D. L. Turner, V. Angelopoulos, and D. M. Malaspina. Quantified energy dissipation rates in the terrestrial bow shock: 1. Analysis techniques and methodology. *Journal of Geophysical Research: Space Physics*, 119(8):6455–6474, 2014. ISSN 2169-9402. doi: 10.1002/2014JA019929.